Ambient seismic wave field

Kiwamu Nishida
Earthquake Research Institute, University of Tokyo,
1-1-1 Yayoi 1, Bunkyo-ku, Tokyo 113-0032, Japan

May 13, 2017

Abstract

The ambient seismic wave field, also known as ambient noise, is excited by oceanic gravity waves primarily. This can be categorized as seismic hum (1–20 mHz), primary microseisms (0.02–0.1 Hz), and secondary microseisms (0.1–1 Hz). Below 20 mHz, pressure fluctuations of ocean infragravity waves reach the abyssal floor. Topographic coupling between seismic waves and ocean infragravity waves at the abyssal floor can explain the observed shear traction sources. Below 5 mHz, atmospheric disturbances may also contribute to this excitation. Excitation of primary microseisms can be attributed to topographic coupling between ocean swell and seismic waves on subtle undulation of continental shelves. Excitation of secondary microseisms can be attributed to non-linear forcing by standing ocean swell at the sea surface in both pelagic and coastal regions. Recent developments in source location based on body-wave microseisms enable us to estimate forcing quantitatively. For a comprehensive understanding, we must consider the solid Earth, the ocean, and the atmosphere as a coupled system.

1 Introduction

Seismometers were developed to record ground motions caused by seismic events such as earthquakes and volcanic eruptions. Even in seismically quiet periods, seismometers record persistent random fluctuations[1)] known as "ambient noise". This noise is not instrumental or local but is ubiquitous irrespective of location. The amplitude of ambient noise is greater along coastal areas than at continental stations. The dominant peak frequency is about 0.15 Hz, which is twice the typical frequency of ocean swell of about 0.07 Hz. The ambient noise around the frequency can be explained as a persistent seismic wave field excited by ocean swell activity and is a significant source of noise in observations of seismic waves from earthquakes.

To avoid the larger amplitudes of the ambient noise, seismologists have developed high-frequency sensors with corner frequencies higher than 1 Hz and low-frequency sensors typically got frequencies lower than 0.1 Hz. Consequently, seismic records have been divided into two categories based on the typical frequency.

In the 20th century, numerous short-period seismometers were installed for earthquake observations. Because of limited digital resources, for many of these seismometers, the recording systems were designed to be triggered by the first arrival of an earthquake. In most cases, continuous data were recorded only by broadband seismometers. Therefore, seismologists omitted ambient seismic wave fields as seismic noise, and these wave fields were merely considered "ambient noise" in seismic observations.

Over the last 20 years, improvements in digital storage and computer networking have enabled us to record continuous seismic data at many seismic stations. Continuous seismograms can now be recorded at more than 1000 stations (e.g. USArray,[2] Hi-net[3]) in near-real time. To utilize "ambient noise" information, a new seismic exploration method has been developed, called seismic interferometry (SI).[4] Cross-correlating seismic records of ambient seismic wave fields between a pair of stations provides information on the impulse response at a station when applying a point force at the other station. Because seismologists have been able to turn this "noise" into signal, we hereafter refer to these observations as the ambient seismic wave field rather than "ambient noise". The theory of SI is based on the assumption of homogeneous and isotropic excitation of seismic waves.[5]Because ocean swell activity varies spatially and temporally, it is not homogeneous or isotropic, and therefore biases travel-time measurements between a pair of stations measured by SI.[6]–[8] Therefore, understanding the excitation mechanisms of the ambient seismic wave field is crucial to improving SI techniques.

The frequency of the ambient seismic wave field ranges from 1 mHz ($= 10^{-3}$ Hz) to 100 Hz. Below 1 Hz, the dominant source of this wave field is oceanic gravity waves (specifically, ocean swell, wind waves, and ocean infragravity waves). These signals are stationary stochastic within approximate time scales of several hours, which correspond to typical time scales for ocean wave activity related to meteorological phenomena such as storms. Based on the typical frequencies of these wave fields, they are categorized into seismic hum (1–20 mHz), primary microseisms (0.02–0.1 Hz), and secondary microseisms (0.1–1 Hz), as shown in Figure 1. This review covers ambient seismic wave field below 1 Hz. Above 1 Hz ambient seismic wavefields are linked to human activities.[9] Although the ambient seismic wave fields above 1 Hz are beyond the scope of this review, they are thoroughly presented in detail in the review by Bonnefoy *et al.* 2006.[9]

The following subsections briefly introduce 20th-century research on this topic

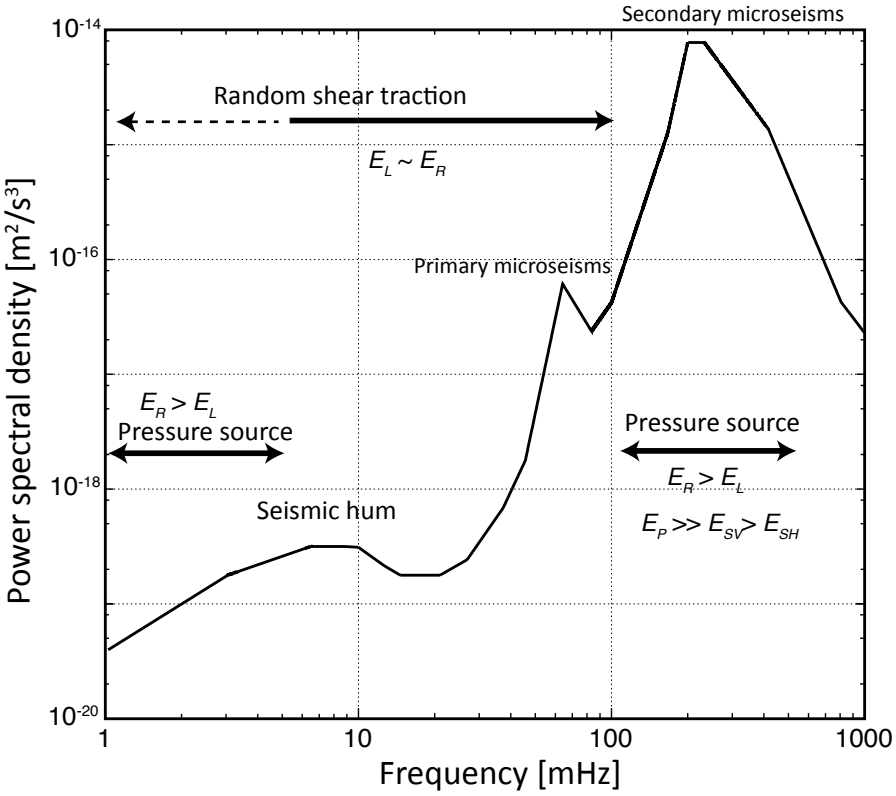

Figure 1: Typical power spectrum of the ambient seismic wave field. The vertical axis shows power spectral densities of ground acceleration. Above 5 mHz, seismic background noise (e.g., the New Low Noise Model (NLNM)[12]) can be explained by the ambient seismic wave field. The force systems of the excitation sources are also shown.[13),14)] Here, E_L is the energy of Love waves, E_R is that of Rayleigh waves, E_P is that of P waves, E_{SV} is that of SV waves, and E_{SH} is that of SH waves.

(for detailed, comprehensive reviews, see for microseisms[10)] and for seismic hum,[11)] for example).

1.1 Microseisms

Observations of microseisms date back to the late 19th century.[1),15)] Since seismologists began observing seismic waves from earthquakes, the existence of an ambient seismic wave field with a dominant frequency of about 0.15 Hz was firmly established. Based on the typical frequencies of these waves, microseisms can be categorized into (1) primary microseisms between 0.02 and 0.1 Hz and (2) secondary microseisms between 0.1 and 0.5 Hz. The former frequency range corresponds to that of ocean swell itself, whereas the latter corresponds to double the frequency of ocean swell.

In the early stage of this research in the late 19th century, seismologists recognized the coincidence of microseismic activities with maritime weather conditions.[1),15)] Under severe weather conditions, microseismic activity increases simultaneously within a spatial scale on the order of 1000 km of the storm.[16),17)] Whether

the source of this excitation was atmospheric or oceanic remained controversial until the 1950s. For example, Gherzi (1945)[18] considered microseisms to be excited by "pumping" of the storm associated with low pressure.[10] Scholte proposed that periodic atmospheric pressure changes at the sea surface generated microseisms.[10] Sezawa and Kanai (1939)[19] also discussed the possibility of atmospheric excitation. Despite the coincidence of microseisms with weather conditions, atmospheric excitation cannot fully explain all observations of these waves.[20]

Another candidate for the source of excitation is ocean swell activity. The earlier hypothesis by Wiechert (1904)[21] was that microseisms are excited by the impact of ocean waves breaking against a steep coast.[17] Omori (1918) also pointed out that ocean swell activity is the most probable sources based on ocean wave height data at coastal stations and seismic observations.[22–24] This hypothesis can explain most observations, but cannot account for the typical frequency of microseisms, i.e., twice the frequency of ocean waves.

Miche (1944) pointed out that pressure fluctuations of standing ocean surface gravity waves can reach the seafloor if the quadratic term of their particle velocity (second-order effects) is included.[25] In contrast, the linear pressure fluctuations of the surface gravity waves (first-order effects) attenuate exponentially with depth. Moreover, the first-order effects are insufficient to excite secondary microseisms because the horizontal wavelengths of secondary microseisms are much longer than those of ocean surface gravity waves. The long wavelengths of the second-order effects are suitable for exciting seismic waves. This mechanism can also explain twice the frequency of ocean waves (see details in subsection 4.3). Longuet-Higgins formulated this excitation mechanism mathematically,[20] and Hasselmann extended the theory to random waves.[10] The mathematical formulation is still feasible for sufficiently accurate to synthesize amplitudes of microseisms based on modern wave action models.[26,27] We note that ocean waves also excite ambient low-frequency acoustic waves as in the case of secondary microseisms called microbaroms.[28–30] These waves can be explained by the second-order effect associated with the moving boundary of the sea surface.[31]

1.2 Seismic hum

In the low-frequency band below 5 mHz, seismic waves (equivalent to the Earth's free oscillation in the frequency domain) are more difficult to excite at observable levels because of their longer wavelengths and higher modal mass. After the 1960 Great Chilean earthquake, which remains the largest earthquake ever recorded by seismic instruments, the first observation of the Earth's free oscillation was reported in the memorial paper "*Excitation of the free oscillations of the earth by earthquakes*".[32]

Since then, the eigenfrequencies of these oscillations and their decay rates have been measured and compiled after large earthquakes. Modern seismic instruments now enable us to detect the major modes of oscillations after earthquakes with moment magnitudes larger than 6.5.

Before this first report in 1961, many geophysicists understood that the eigenfrequencies of the modes were key for inferring the Earth's geophysical properties, following Lord Kelvin's estimation of the molten Earth.[33),34)] To detect these oscillations, Benioff *et al.* (1959) analyzed seismographs not only of huge earthquakes but also of seismically quiet intervals,[35)] which are now recognized to represent the Earth's background free oscillations or seismic hum. Benioff *et al.* (1959) evaluated the possibility of atmospheric excitation of Earth's free oscillations but did not discover evidence of this phenomenon.[36),37)] The signal was too weak to detect with the technological accuracy achievable at that time.

Using dimensional analysis for atmospheric excitation based on the theory of helioseismology,[38)] Kobayashi (1996) estimated the amplitudes of seismic hum.[39)] With modern broadband seismometers, these amplitudes can now be observed to the order of 1 ngal (10^{-11} m s^{-2}).[12)] Because a similar mechanism would be anticipated on solid planets, the possibility of Martian seismology has been investigated.[40)–42)] These theoretical predictions triggered searches for seismic hum.

Based on the theoretical estimations, Nawa *et al.* (1998) reported modal peaks of seismic hum recorded by a superconducting gravimeter at Syowa Station, Antarctica.[43)] This discovery triggered debate because distinct peaks could also be caused by seiches in Lützow-Holm Bay, Antarctica.[44),45)] Following this report, seismic hum was also confirmed by different instruments: a modified LaCoste Romberg gravimeter,[46)] an STS-1Z seismometer,[40),47)] and an STS-2 seismometer.[48)] For these studies, the contributions of large earthquakes (typically larger than M_w 5.5) were carefully excluded using earthquake catalogs.[49),50)] The observations of seismic hum by the LaCoste Romberg gravimeter extend back to the 1970s.[46),51)] For the previous 20 years, seismic hum had been accepted as merely observational background noise, although microseisms above 0.05 Hz were already recognized as the background seismic wave field excited by ocean swell activities since the pioneering work by Gutenberg in the 1910s.[52),53)] The observed dominance of fundamental modes and seasonal variations[50),54),55)] suggest that the source of seismic hum is atmospheric or oceanic disturbances.

To evaluate the excitation mechanism of seismic hum, an important observation is the coupling between the solid Earth and atmospheric acoustic waves. The spectra of seismic hum show excess amplitudes at 3.7 and 4.4 mHz.[54)] The two peaks were observed during the major eruption of Mt. Pinatubo in 1991.[56)–58)] These peaks can be explained by acoustic resonance between Rayleigh waves propagating in the

solid Earth and low-frequency acoustic waves in the atmosphere.[59] This observation suggests that atmospheric sources such as cumulus convection contribute at least partially to this excitation.[40),60),61]

2 Source distribution of the ambient seismic wave field

In the following sections, we summarize recent results of the observed source distributions and the energy partitions among wave types of the ambient seismic wave field. Based on these results, we then discuss the physical process of excitation.

The source distribution of the ambient seismic wave field is crucial for characterizing the excitation mechanisms. In particular, the source extent, whether coastal (shallow) or abyssal floor (deep), is key for understanding the physical mechanisms based on the typical frequency. Comparison with an ocean wave action model is feasible, as discussed in the final section.

For determining source locations, four techniques are used: (1) beamforming of the ambient seismic wave field,[62] (2) mapping source distribution by backprojecting observed body waves based on travel time, known as the backprojection method,[63] (3) modeling cross-correlation functions between pairs of stations, and (4) polarization analysis of Rayleigh waves at a station.[64] Although the former three methods are similar, in practice, each of these methods provides different information based on the different assumptions applied, as shown below. In the final subsection, the inferred source distributions are summarized based on typical frequencies.

2.1 Beamforming

A beamforming method[62),65),66] with a dense seismic array can feasibly be used to locate the sources of microseisms[67),68] and seismic hum.[69)–72] Under the assumption that a seismic wave field can be represented by the superposition of plane waves, the power of the waves can be decomposed. We also assume that lateral heterogeneities of the seismic structure beneath the array are small. First, we assumed a slowness vector ($\boldsymbol{k}/\omega$, where $\boldsymbol{k}$ is the wavenumber vector, and ω is the angular frequency) for a plane wave. With estimated time shifts to a reference point according to the geometry of the station and the slowness vector, the seismograms are stacked over all traces. The mean-squared (MS) amplitude of the stacked seismogram against the assumed slowness vector is then calculated. The MS amplitudes plotted against every slowness vector within a two-dimensional slowness domain show a bright spot if a simple plane wave was incoming. Because the number of stations is finite, the bright spot is broad and smeared, which can be characterized by the array

response function.[62] For many incoming plane waves, the beamforming results show distributions with peaks at the corresponding slowness vectors.

Figure 2 shows typical example results of beamforming for seismic hum at 0.0125 Hz.[14] Figure 2(b) shows clear Love (top panels) and Rayleigh (bottom panels) wave propagations. The propagations from the ocean are dominant, whereas those from the continent are too weak to detect. In particular, propagations along the coast are larger.

Based on observations of multiple arrays, triangulation results indicate source locations. Above 0.05 Hz, complex seismic propagations of surface wave distort the beamforming results frequently. In the secondary microseismic band, thick sedimentary layers affect surface wave propagation significantly.[73] Accretionary wedges are often obstacles for locating source distribution because on-land stations are typically surrounded by them. Because the S-wave velocities through such layers are typically slower than 1.0 $\mathrm{km\,s^{-1}}$, Rayleigh waves tend to be trapped in sedimentary basins. Scattering and trapping homogenize the azimuthal distribution of propagation directions. Although this condition satisfies the assumption of equipartition of modal energy for seismic interferometry,[74] it means that source information is lost due to scattering. In the primary microseismic band, we note that a deep water column along an ocean trench causes considerable reflection and refraction of Rayleigh wave propagation,[75),76] which could bias the results (see also subsections 3.1 and 3.2). Below 0.05 Hz, these effects weaken because the sedimentary layer is thin enough relative to the wavelength of the surface waves.

2.2 Backprojection method

A backprojection method is a powerful tool for locating the source of microseisms when travel time can be inferred accurately with a seismic velocity model. The backprojection method has been developed to infer the source processes of large earthquakes. Using dense array data from several hundred stations, P-wave records are typically backpropagated to the source region with a reference 1-D Earth structure.[63),77] To suppress the biases caused by the 3-D seismic velocity structure, station correction terms are reduced using well-located earthquakes if possible. In principle, the slowness of P waves constrains the epicentral distance between the centroid of the source and the array locations. With the back azimuth of observed P waves, source locations can be inferred. In particular, if the typical spatial scale of the array is long enough (typically longer than 1000 km), slight variations of the slowness vector within the array enable better constraint of the source location.

The advantage of this method is higher resolution of the centroid locations where high energy radiates. Sufficient spatial resolution is crucial for quantitative compari-

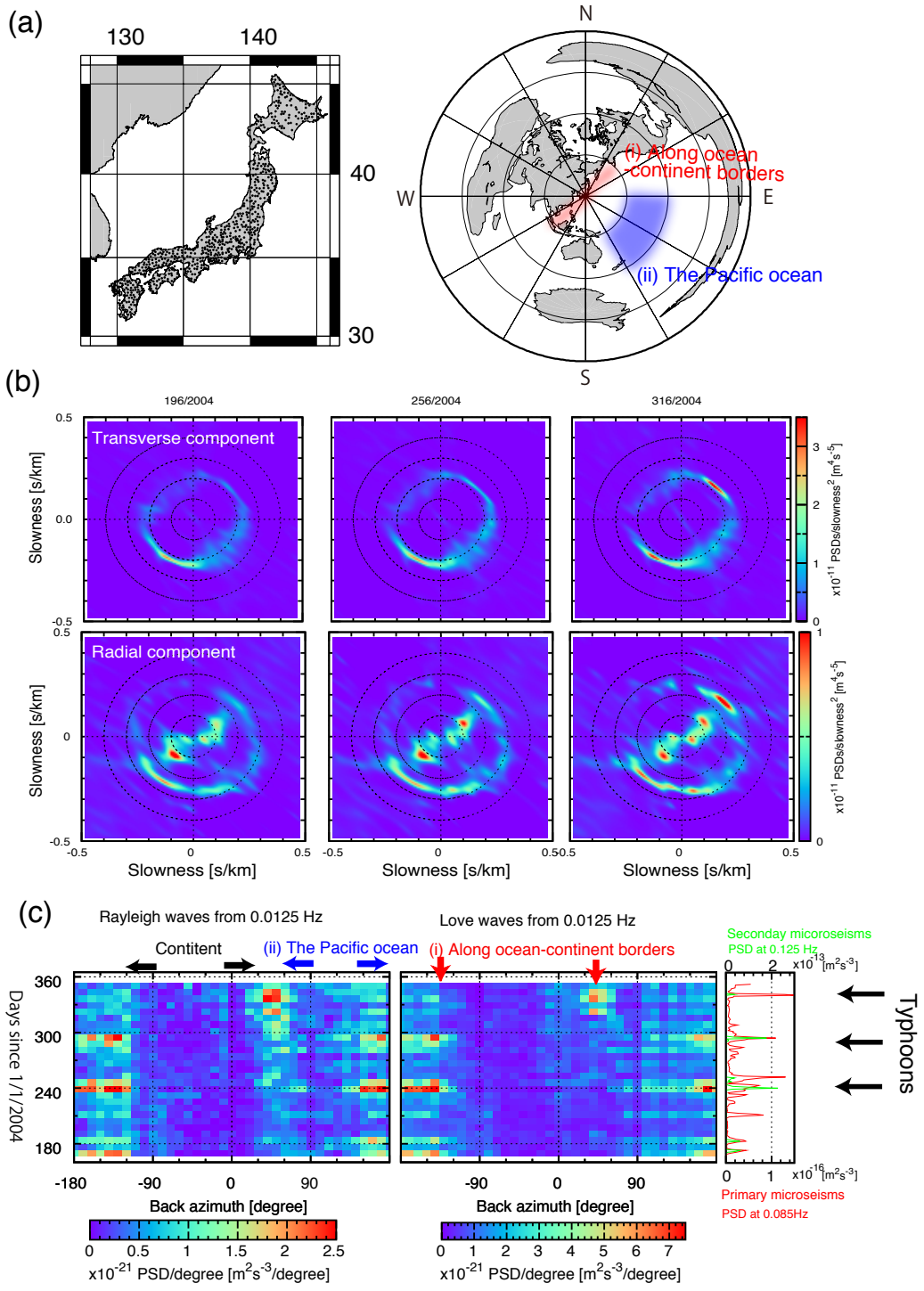

Figure 2: (a) Location map of 679 Hi-net tiltmeters and the distribution of continents and oceans in the azimuthal projection from the center of the Hi-net array. (b) Beamforming results at 0.0125 Hz, calculated for every 60 days from 166/2004-346/2004. (c) Azimuthal variations of Love and Rayleigh wave amplitudes at 0.0125 Hz as a function of time showing similar azimuthal patterns. The right column indicates the temporal change of amplitudes of primary microseisms (mean power spectral densities from 0.08 to 0.09 Hz), and secondary microseisms (those from 0.12 to 0.125 Hz) showing activity patterns similar to those of Love and Rayleigh waves at 0.0125 Hz. This figure is reproduced from Figures 1 and 2 of Nishida *et al.* (2008).[14)]

son with wave height data. A drawback is a difficulty of estimating the spatial extent of the source because of the limited spatial extent of the dense array. Although the centroid locations can be precisely located, this method tends to lose information on the source extent.

The backprojection method can be used for teleseismic body waves of secondary microseisms.[78)–85)] Complex wave propagations of surface waves above 0.05 Hz caused by strong shallow, lateral heterogeneities make it difficult to locate the excitation sources by backprojecting surface waves. However, body wave microseisms propagate in the mantle, which is much more transparent than the crust. Body wave microseisms tend to be scattered less during propagation, although the excited amplitudes of teleseismic body waves are much lower than the amplitudes of surface waves. The weak scattering enables us to estimate the excitation term precisely based on a simple 1-D seismic velocity model. This method provides rich source information.

A point source approximation is feasible for characterizing the sources in this case because the source area is distant from the stations. This approach is based on the assumption that the random excitation sources on the Earth's surface are characterized by multipole expansion of the force distribution.[86)] Therefore, the equivalent body force acting on the centroid location of the monopole can be estimated.[85)] Figure 3 shows their precise locations of P-wave microseisms at 0.15 Hz based on data at about 700 Hi-net stations in Japan[3)] when a "weather bomb" was generated in the Atlantic Ocean in 2015. This method can provide information about the force system at a macroscopic scale. The force system is recognized as the equivalent force, which is coarsened by the long wavelengths of seismic waves. In this case, the sources can be characterized an equivalent vertical single force at the centroid location as discussed in subsection 4.3. On the other hand, the excitation sources of primary microseisms and seismic hum could be characterized by an equivalent horizontal single force as discussed in subsections 4.1 and 4.2.

Body-wave amplitudes of primary microseisms and seismic hum are too weak for the backprojection method. However, in the frequency range of the seismic hum, this method is also applicable for seismic surface waves.[70)] The wave propagation can be predicted with a one-dimensional Earth model because it is insensitive to lateral heterogeneities with smaller spatial scale than the wavelength. Above 0.02 Hz, the simple model cannot predict seismic surface wave propagations because of strong lateral heterogeneity in the crust and the distribution of land and sea. The resulting complex wave propagation causes destructive interference in seismic records.

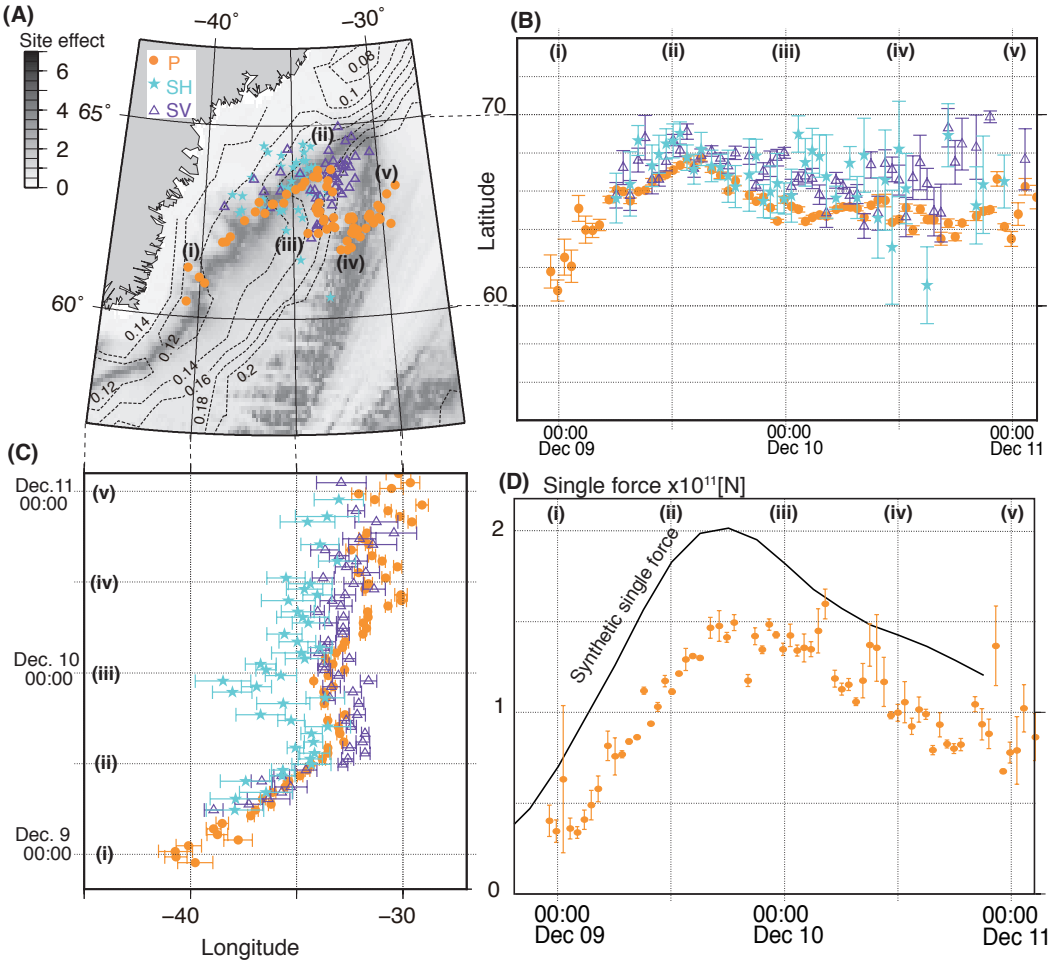

Figure 3: (a) Locations of centroids with smaller bootstrap errors of 1.5° in latitude and longitude. Orange dots indicate the centroids of P-wave microseisms. Purple triangles indicate SV-waves. Blue stars indicate SH-waves. The background image shows the site effect of the ocean layer, whereas the contours show the resonant frequency of the sediment. The resonant frequency was estimated based on the four-way travel time of multiple reflections of sediment-derived S-waves in the vertical direction. (b) Latitude of centroids of P-, SH-, and SV-waves with respect to time. (c) Longitude of centroids with respect to time. (d) Temporal variations of root-mean-square amplitudes of the single force. Taken from Figure 2 of Nishida and Takagi (2016).[85)]

2.3 Cross-correlation function-based method

Another strategy for source location is data analysis using cross-correlation functions (CCFs) between pairs of stations. Here, we consider a CCF of seismic records between station 1 and station 2. The sensitivity kernel of a CCF for source distribution is confined along the major arc of the station pair. The causal part of the CCF (positive lag time) has higher sensitivity along the major arc to the station 1 side, whereas the acausal part (negative lag time) has higher sensitivity to the station 2 side.[5)] By collecting CCFs between a reference station and other stations, we can infer the azimuthal distributions of propagation directions for the reference station. We note that CCFs in the frequency–wavenumber (FK) domain represented by Bessel expansion[87),88)] are convenient for seismic array data, although the formulation in a 1-D seismic structure is mathematically equivalent to the representation in the spatio-temporal domain. The spectrum with respect to the order of Bessel functions shows the incident-azimuthal distribution of incoming seismic waves.

In the frequency range of seismic hum below 10 mHz, the weaker lateral heterogeneities of the surface waves associated with long wavelengths enable us to synthesize CCFs based on the normal mode theory with a reference 1-D structure.[61),89)] The sensitivity kernel of a CCF for a given source distribution[89),90)] is primarily sensitive along the major arcs, whose shape can be characterized by a hyperbola with foci at the pair of stations because of finite frequency effects. Using the kernel, the source distribution can be inferred by minimizing the squared differences between the observed CCFs and the synthetic CCFs.[89)] The results are consistent with those obtained from the backprojection method,[69),72),91),92)] as described in subsection 2.5. The recent development of numerical methods enables us to synthesize CCFs based on a 3-D model,[93)] to avoid trade-offs between the uncertainty associated with seismic structures and the source distribution. With increasing the frequency, this method becomes unrealistic, because this method is too sensitive to the uncertainties of the lateral heterogeneities.

Mapping the energy of the CCFs onto the major arcs is feasible for a source location using sparsely distributed stations at the higher frequency.[94)] This method is particularly feasible for locating sources using surface wave propagation for frequencies above 0.05 Hz because it is less sensitive to uncertainties associated with strong lateral heterogeneity in the crust than the beamforming method is. Although this method is robust to the lateral heterogeneities even at the higher frequency, the spatial resolution is lower than that of the other methods.

2.4 Polarization analysis

Although the methods described above are effective tools for source localization, they require data from multiple stations. At a global scale, such arrays remain sparsely distributed, especially in the southern hemisphere. In this case, a single-station analysis is more applicable in practice. When Rayleigh wave excitation is dominant, polarization analysis can be used to determine the incident azimuth.[64),65)] The particle motion of Rayleigh waves can be described as retrograde elliptic motions within a vertical plane along the source–receiver path. The polarization can be estimated through eigen analysis of the covariance matrix between the vertical and horizontal components.

2.5 Summary of observed source distribution

Based on the different observations, we summarize here the observed source distribution based on the frequencies of seismic hum, primary microseisms, and secondary microseisms.

For seismic hum, all of the results, including the beamforming results of Love and Rayleigh waves,[14),69),72),91),92)] the backprojection of Rayleigh waves,[70)] and CCF analysis, show a dominant source area located in the North Pacific Ocean from July to September, and in the Antarctic Ocean from December to February. These results also show that excitation on land is negligible. Some studies have proposed dominant sources in shallow coastal areas,[70),72),92)] which would suggest nonlinear interactions at shallow depths. However, our findings indicated source distributed on the deep-seafloor.[89)] Beamforming results[89)] also support this observation. For example, Figure 2 shows the significant energy of Love and Rayleigh waves from the abyssal floor with back-azimuth from 120° to 150°, especially around days 170, 240, and 300 in 2004, which correspond to major typhoons. Although source localization remains controversial, we can conclude that stronger sources are in coastal areas and weaker sources are distributed on the deep seafloor.

Major difficulties in source location originate from poor signal-to-noise ratios.[12),95)] Observation of the very low power spectral densities of about 10^{-19} [m^2s^{-3}] remains challenging. In particular, horizontal components in the mHz frequency range are much noisier than those of vertical components in the same range because the former are too sensitive to local tilt motions induced by, for example, meteorological events.[96),97)] Sparse station distribution in the southern hemisphere is also problematic, although this situation has been recently improved.

In the frequency range of primary microseisms, sources were located in shallow coastal areas, based on beamforming analysis[67),68),72),98)–100)] and CCF analysis[101),102)] of the Love and Rayleigh waves. The dominant source in Europe is the

near-shore region of the North Atlantic Ocean.[67),68),100),103)] Strong primary microseisms excited in the North Atlantic Ocean can reach Japan over continental paths.[104)] Other major sources are the west coast of North America[67),72)] and Polynesia in the South Pacific.[72)] The source locations of Love and Rayleigh waves are coincident with each other at a large scale,[14),99),100)] although there are significant differences between them.[100),104),105)]

Difficulties in source location using surface waves in the primary microseismic band are caused by complex wave propagation. Although source location based on teleseismic body wave microseisms has a superior spatial resolution because of relatively simple wave propagation, the signals in this frequency range are too weak to use.[106)] The lack of teleseismic body waves may be caused by the excitation mechanism, as discussed in a later section.

A clue for the source localization of primary microseisms is the observation of precursory signals for a CCF between a land station and an ocean floor station, which emerge before the first arrivals when strong localized sources exist in near-shore areas between the pair of stations. Tian and Ritzwoller (2015) pointed out the importance of precursory signals. They analyzed CCFs using data from ocean floor seismometers on the Juan de Fuca Plate from the Cascadia Initiative experiment and from continental stations near the west coast of the United States.[102)] The observed precursory signals suggest spatially stable radiation patterns of the surface waves, which may be frozen to the topography there. Although the precursory signal is often observed in the primary microseismic band, CCFs of seismic hum does not show clear signals.[89),107)] The absence of a strong precursory signal suggests that the sources of seismic hum may be distributed on more broad areas of the ocean floor. To improve source localization, more sophisticated numerical methods should be developed that include these complex seismic propagation behaviors.

For the frequency range of secondary microseisms, using both beamforming and CCF analysis of observed Rayleigh waves, sources were located in both near-shore[67),101)] and pelagic areas[67),102),108)] . Most studies have shown seasonal variations in the amplitudes of these microseisms. At a global scale, strong excitation sources exist in the North Pacific Ocean from July to September, and in the Antarctic Ocean from December to February[81),109),110)] (Figure 4), because high swell activity is expected in winter months. Polarization analysis[26),64),65)] also supports this global pattern. At local and regional scales, these changes are correlated with storm activity. The estimated source distribution was consistent with a theoretical estimation based on wave action models, which hindcast frequency–directional spectra of wind waves including contributions by local wind and distant weather systems.[26),27),81),83),111)–114)]

Details of the excitation depend on individual storm events and the frequency

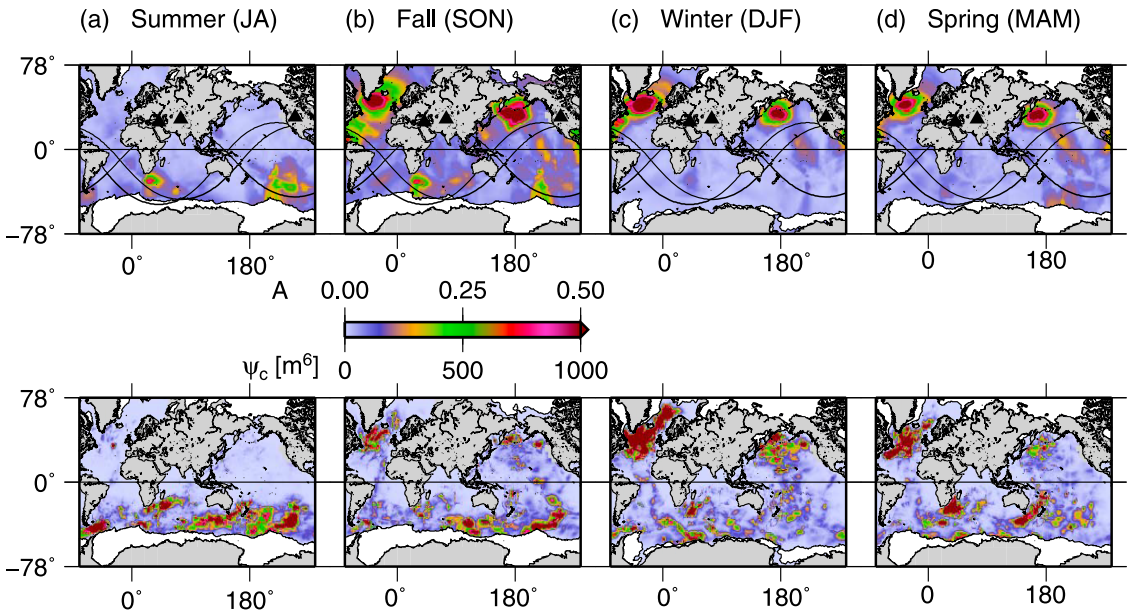

Figure 4: The (top) observed and (bottom) predicted global excitation patterns can serve as a template for future investigations of global microseism hot spot activity. Each pixel is occupied by the maximum of the wave-wave interaction modulated by bathymetry Ψ_c and seismological observation A measured during the corresponding season. Seasons are associated with the Northern Hemisphere. Letter combinations indicate months: JA, July, August; SON, September, October, November; DJF, December, January, February; and MAM, March, April, May. From Figure 10 of Hillers *et al.* 2012.[81)]

range. For example, observations from an ocean-floor seismic station at 4,977 m depth halfway between Hawaii and California showed that secondary microseisms in pelagic and coastal regions depend on their typical frequency. Below 0.2 Hz, sources in coastal areas are dominant, which suggests the importance coastal reflections of ocean swell, whereas, above 0.2 Hz, sources in pelagic areas are dominant, which are excited by local wave–wave interaction above the station.[115)] Beamforming based on teleseismic P waves also shows that secondary microseisms were generated in both pelagic and coastal regions. For example, when Typhoon Ioke was developed in the Central Pacific in 2006, beamforming results using seismic arrays in Japan and California show the dominant sources in the deep ocean from 0.16 to 0.35 Hz, and dominant sources in near-shore regions close to Japan from 0.1 to 0.15 Hz[79)]). Based on beamforming analysis using a seismic array in Australia,[110)] P-wave source locations are also identified from 0.1 to 0.5 Hz in deep-ocean regions (in the southern Indian Ocean) and in shallow waters from 0.5 to 0.7 Hz (in the Great Australian Bight, the Kerguelen Plateau, and the east coast of Japan for frequencies by a small span array in Australia). The pelagic sources from 0.1 to 0.5 Hz are also detected in the North Atlantic Ocean,[84),85),114),116)] in the Sea of Okhotsk and[110)] in the North

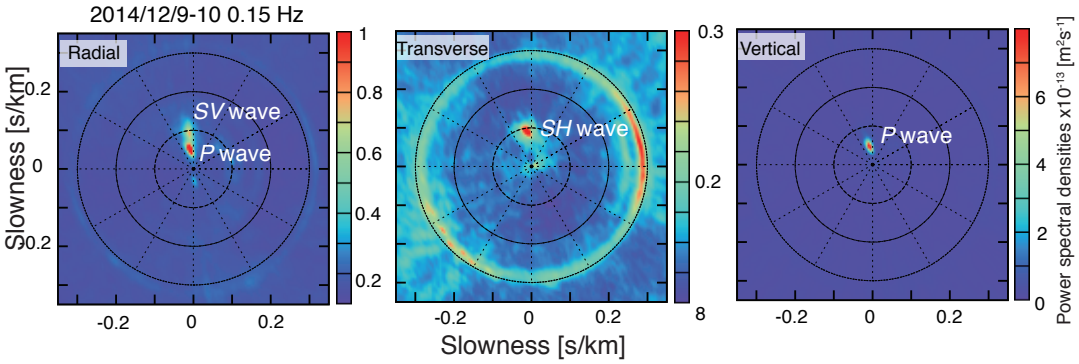

Figure 5: Beamforming results for the radial, transverse, and vertical components at 0.15 Hz. This figure shows a P-wave traveling from the north with a back azimuth of about -7°. The slowness is about 0.048 s km^{-1}, which determines the distance between the source and the receivers. From Figure 1 of Nishida and Takagi (2016).[85)]

Pacific Ocean.[84),114)] Polarization analysis at stations in the Indian Ocean[117)] from 0.09 to 0.17 Hz supports the pelagic sources in the southern Indian Ocean.

Based on data from seismic arrays in Japan and China, beamforming results from 0.1 to 0.4 Hz showed not only P- but also S-wave microseisms excited by a severe, distant storm in the Atlantic Ocean[85)] (Figure 5), North Pacific, and Indian Oceans.[84)] Backprojection results based on data in Japan showed their precise centroid locations of P- and S-wave microseisms in the Atlantic Ocean[85)] (Figure 3). The inferred centroid locations of P-wave and vertically polarized S-waves (SV-waves), and the inferred equivalent vertical single force were consistent with a wave action model; they migrated along a depth contour of about 3000 m depth, which can be attributed to the resonance of the water column at that depth.[118)] This phenomenon can be described as the constructive interference of P-wave multiple reflections in the oceanic layer. Amplification due to resonance becomes larger where the resonance frequency of the oceanic layer matches the double frequency of ocean swell. In contrast, the centroids of horizontally polarized S-waves (SH-waves) stayed in the thick sedimentary area. The source locations of SH-waves revealed that they are converted from SV-waves during multiple reflections in the thick sediment where the sedimentary resonant frequency matches the oceanic resonant frequency.

3 Energy partitioning among seismic wave types

Although source distributions provide information about excitation sources, the results cannot fully constrain the physical processes of that excitation. Energy partitioning among seismic wave types gives a further clue for understanding these processes.[14),85),119),120)] In this section, we summarize observations of energy partitions (i) between fundamental modes and overtones, (ii) between Love and Rayleigh

waves, and (iii) between P-SV and SH waves based on typical frequencies.

3.1 Fundamental modes and overtones

In general, across the entire frequency range, the modal energy values of the fundamental toroidal and spheroidal modes (Love and Rayleigh wave equivalently) are larger than those of the overtones. The observed dominance of the fundamental modes indicates that the excitation source should be located at the surface or just below the surface. Details of energy partitioning according to the frequencies are summarized below.

First, for the energy partitioning of seismic hum, Figure 6 (a) shows the observed frequency–wavenumber (FK) spectra in vertical–vertical components (ZZ), radial–radial components (RR), transverse–transverse components (TT), and vertical and radial components (RZ).[121] These spectra show dominance of the fundamental modes (Love and Rayleigh waves equivalently). They also show weak but clear overtone branches. TT shows a weak but definite first overtone branch of Love waves, whereas ZZ and RR show branches of overtones expressed as several lines. These waves are a type of surface wave trapped within the crust and/or the uppermost mantle, which are known as shear-coupled PL waves.[122),123] These waves can be excited effectively by a source of shear traction at the surface, as shown in Figure 6(c). The corresponding beamforming results for the radial component shown in Figure 2 support these observations. Although the amplitudes of body waves in the FK domain, which propagate into the deep Earth, are weaker than the overtones of the surface waves, their spatio-temporal representation (stacked CCFs binned according to separation distance)[123] shows weak but clear teleseismic body wave propagation, which is consistent with the source of surface traction.

FK spectra above 0.05 Hz in Japan[127] (Figure 7) also show dominance of the fundamental modes. The FK spectrum of RR shows a clear branch of crustal P waves (Pg) (Figure 7 (a)), as well as a weak first overtone branch of Rayleigh waves, which was also observed from 0.14 to 0.25 Hz at an array in New Zealand.[128] However, the FK spectrum of TT shows the first and second overtones of Love waves above 0.1 Hz, the energy of which is trapped in the crust (Figure 7 (b)).

Whereas the energy of the fundamental modes is dominant above 0.15 Hz at coastal stations as shown in Figure 7 (near the Pacific Ocean), the energy of the overtones becomes dominant at inland stations at frequencies above 0.15 Hz. For example, an inland array in Kazakhstan[120] shows dominance of body waves and overtones from 0.15 to 0.3 Hz. Another inland array in the United States[99),119] also shows the dominance of overtones above 0.2 Hz. An inland array of vertical seismometers that spans 25 km in Australia[110] shows dominance of fundamental

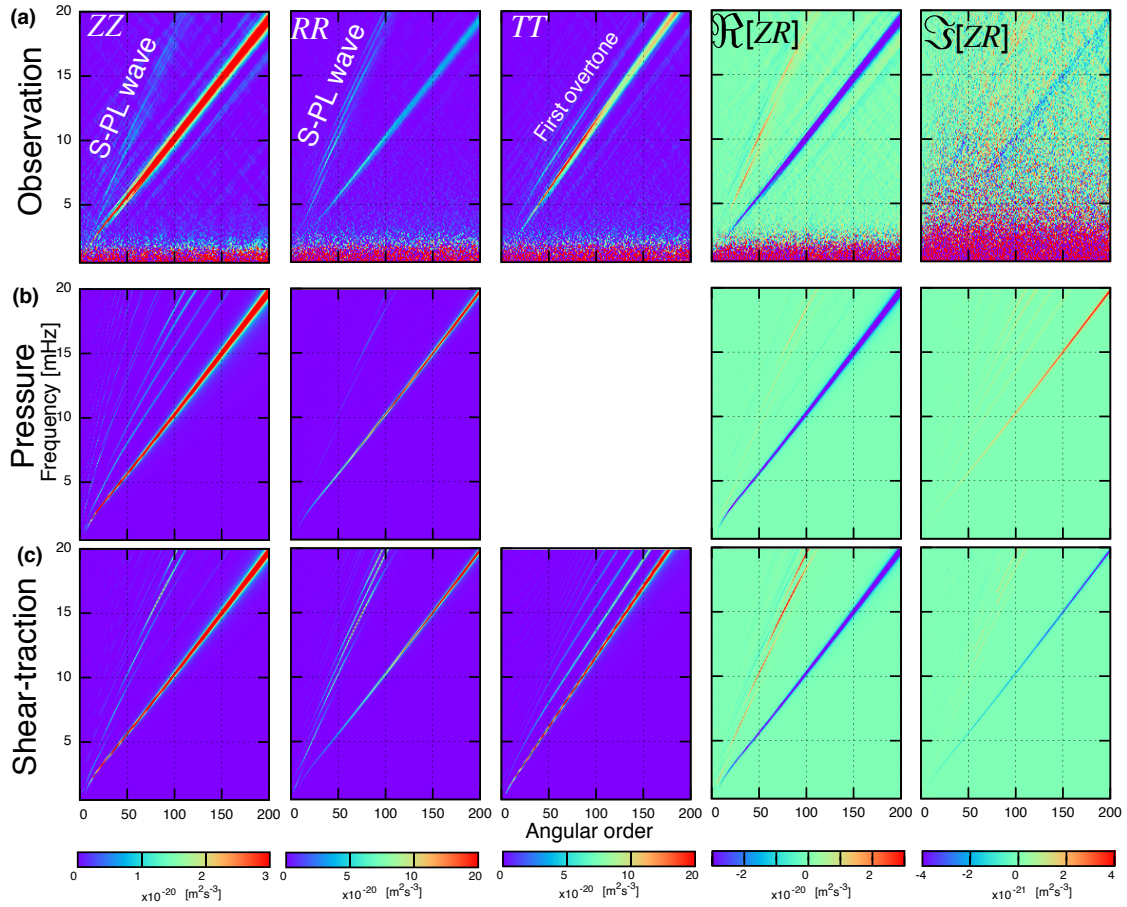

Figure 6: (a) Observed FK spectra of the vertical–vertical component (ZZ), the radial–radial component (RR), the transverse–transverse component (TT), and the real ($\Re[]$) and imaginary ($\Im[]$) parts of the vertical–radial component (ZR) against angular order l and frequency. The amplitudes of the FK spectra plot at frequencies and corresponding wavenumbers estimated by modeling CCFs of each pairs of stations using Bessel or Legendre functions[124),125)] based on the assumption of homogeneous and isotropic excitation of the seismic wavefield.[124)] This method is a natural extension of the spatial auto-correlation (SPAC) method proposed by Aki.[126)] (b) Synthetic FK spectra for pressure sources. These pressure sources cannot explain the observed Love wave excitations or the observed overtones of spheroidal modes. The model also cannot explain the imaginary part $\Im[ZR]$. (c) Synthetic FK spectra for shear traction sources. These spectra can explain even the observed overtones and the observed imaginary part $\Im[ZR]$. This figure is from Figure 3 of Nishida [2014].[121)]

Rayleigh waves from 0.3 to 0.5 Hz, and dominance of overtones from 0.5 to 0.7 Hz. For the northern Fennoscandian region, cross-correlation analysis of high-frequency secondary microseisms reveals Moho-reflected body wave (0.5–2 Hz)[129] and P waves reflected by the 410 and 660 discontinuities (0.1–0.5 Hz)[130] for inter-station distances up to 550 km. The Moho-reflected body waves were also observed at inland seismic arrays at Yellowknife in north Canada, Kimberley in south Africa[131] and the Sierra Nevada in the United States[132] above 0.5 Hz.

The dominance of overtones is attributed to differences in the propagation characteristics between surface waves and body waves. The excited amplitudes of body wave microseisms are smaller than the amplitudes of surface waves in the source area. In contrast, at inland stations, surface waves with frequencies above 0.1 Hz are attenuated by scattering during propagation from ocean because of strong lateral heterogeneities in the crust, with a mean free path on the order of 100 km.[133] Surface waves above 0.1 Hz are also easily trapped at marine sediments such as accretionary prism. Even if they can reach to the land, their amplitudes are highly attenuated. However, the overtones are scattered less because they are sensitive to deeper mantle structures, which are less heterogeneous. For example, the scattering mean free path of teleseismic body waves in the mantle is on the order of 1000 km.[134] When the distance between a station and the source area of microseisms is longer than 30°, P-wave microseisms are generally dominant above 0.2 Hz.[120]

Even at coastal stations, overtones and teleseismic body waves become dominant in the frequency range of secondary microseisms when local ocean swell activity is calm and distant swell activity is intense. An example of this case is recorded in Hi-net data in Japan when a low-pressure weather system hits the Atlantic Ocean[85] (Figure 5). Another example may be observations of the first overtone of Rayleigh waves at 0.15–0.2 Hz from west-northwest observed in the Netherlands[103]

At low frequencies of seismic hum, the effects of ocean layers on wave propagation are secondary because the ocean depth is much less than the wavelength. With increasing frequency, the wavelength becomes comparable to the depth. In pelagic regions, fundamental oceanic modes exist above 0.05 Hz. The energy partition between the fundamental oceanic mode and the overtones is a clue for inferring the source depth. The oceanic fundamental mode with phase velocity of around 1.5 $\mathrm{km\,s^{-1}}$, also known as a Scholte–Rayleigh wave,[135] is trapped within the ocean layer above 0.05 Hz, whereas the first overtone above 0.1 Hz is sensitive to the structure of the crust and uppermost mantle, similar to a continental Rayleigh wave. However, estimating the energy partitioning is impossible from on-land observations because Scholte–Rayleigh waves cannot exist without the ocean. In-situ offshore observations of secondary microseisms are indispensable for this estimation. Some researchers[136]–[139] have observed multiple modes from ocean-bottom seismometers

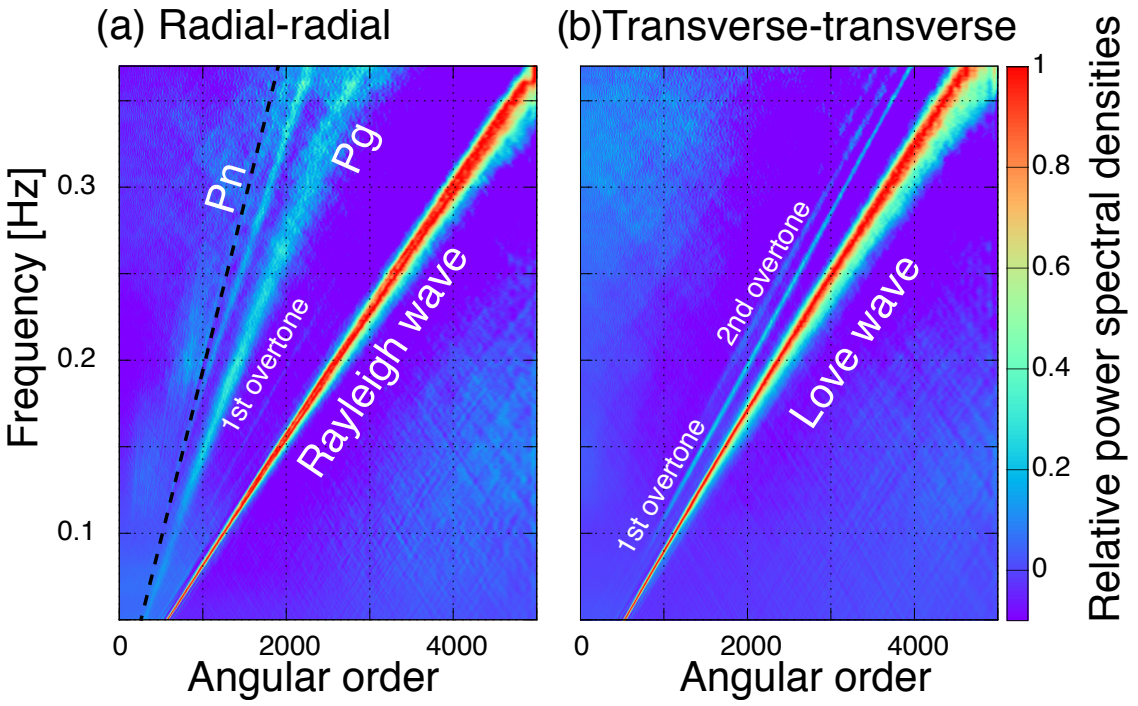

Figure 7: FK spectra of (a) the radial–radial component and (b) the transverse–transverse component calculated from CCFs between Hi-net tiltmeters in Japan.[127] Power spectral densities are normalized based on the maximum value at each frequency. The panels show that the overtone amplitudes are one order of magnitude smaller than the fundamental mode amplitudes. This figure is reproduced from Figure 6 of Nishida *et al.* (2008).[127]

in the deep ocean (3-5 km). From 0.05 to 0.1 Hz, the fundamental spheroidal mode (oceanic Scholte–Rayleigh wave) is dominant because energy leakage of the overtones into the mantle suppresses their amplitudes. From 0.1 to 0.2 Hz, all results show the fundamental mode and the first overtone. The larger amplitude of the fundamental spheroidal mode suggests a deep-ocean excitation source because the mode exists only in pelagic regions.[76] At frequencies higher than 0.2 Hz, the second overtone is also observed[138] as anticipated based on theory.[76]

At higher frequencies (typically above 0.2 Hz for 5 km depth), the higher oceanic spheroidal modes[76] cause complex wave propagation. Soft sediments, such as accretionary prisms, also complicate wave propagation.[140]

3.2 Energy partitioning between Love and Rayleigh waves

The kinetic energy ratio of Love to Rayleigh waves is key to understanding the forces system. The dominance of Rayleigh waves suggests a pressure source in the ocean, whereas dominance of Love waves suggests shear traction at the seafloor. In this subsection, we summarize observed energy partitioning between Love and Rayleigh waves, which are dominant in the ambient seismic wave field.

First, let us consider the ratio of Love to Rayleigh waves of the seismic hum. The FK spectra of seismic hum[125] (Figure 6(a)) show that Love wave amplitudes are larger than those of Rayleigh waves above 5 mHz. Beamforming results from 0.01 to 0.02 Hz[14] (Figure 2) also support this observation. With consideration for the eigenfunctions of 1-D structure, these results exhibit equipartition of kinetic energy between Love and Rayleigh waves. In contrast, a careful single-station analysis[141] showed that kinetic energy of the Love waves is larger than that of Rayleigh wave amplitudes from 3.5 to 5.5 mHz based on auto-correlation analysis.[142] This observation is also supported by the FK analysis.[125] Although horizontal ground motions are, thus, crucial for determining the excitation mechanism, observing these motions at frequencies below 10 mHz is still difficult. The observed Lagrangian horizontal ground accelerations include not only horizontal ground accelerations but also local tilt motions caused by apparent changes in gravitational acceleration. Local noise, such as air pressure, disturbs horizontal seismic records.

At frequencies from 0.005 to 0.1 Hz, beamforming results yield kinetic energy ratios of Love to Rayleigh wave (E_L/E_R) ranging from 0.6 to 2.0, which is larger than 1 on average.[14),100),125] All observations suggest that the force system is dominated by surface shear traction at the seafloor (the corresponding synthetics below 0.05 Hz are shown in Figure 6(c)). The force system can be attributed to topographic coupling between the seismic waves and ocean waves (i.e., infragravity wave at the ocean floor for seismic hum,[13),143] and to ocean swell in near-shore areas for primary

microseisms.[14] see details in the next section). The relative directional amplitude distributions differ between Love and Rayleigh waves in the primary microseismic band.[100] These differences may reflect the effects of the different radiation patterns of Love and Rayleigh wave excitation at the seafloor.[100] In order to clarify the mechanism, more global observations are required because the current observations were limited only sparse area.

Above 0.1 Hz, the kinetic energy ratio of Love to Rayleigh waves (E_L/E_R) ranges from 0.4 to 1.2, based on beamforming analysis[14),100),144] and analysis of data from rotation sensors and seismometers.[145),146] The ratio is generally smaller than 1 at coastal stations. The observed dominance of Rayleigh waves can be explained by the dominance of pressure sources, as expected based on the Longuet-Higgins theory.[20] At on-land stations, an increase in the Love to Rayleigh wave ratio was found for specific source directions in central Europe.[100] The increase in the value of this ratio with increasing propagation distance may be attributed to conversion between Love and Rayleigh waves caused by scattering in the heterogeneous crust. This scattering tends to homogenize the energy partitioning between Love and Rayleigh waves.[100),144]

A major cause of this scattering is the water column, such as in an ocean trench. When Rayleigh waves propagate between the ocean and continent, the water column causes considerable reflection and refraction above 0.05 Hz. Below this frequency, oceanic and continental mode branches need not be differentiated because the wavelength is sufficiently long relative to the depth of the seafloor. The water column thus complicates wave propagation from ocean to land.[75),76] Here we consider the behavior of Rayleigh waves at 0.05 Hz. In a shallow oceanic area (∼100 m depth), oceanic Scholte–Rayleigh waves need not be distinguished from continental Rayleigh waves. However, along a trench, the ocean is deep enough to differentiate these types of wave. The oceanic Scholte–Rayleigh waves tend to be trapped low-velocity areas along ocean trenches.[147)–149] Although conversion from Rayleigh to Love waves must be considered, this conversion is quite complex. The energy partitioning between Love and Rayleigh waves associated with complex wave propagation must be considered. Soft sediments in the ocean, such as in an accretionary prism, further complicate propagation.[140] To more precisely locate sources of Rayleigh wave propagation, this complexity must be considered. Source locations should be evaluated using a sophisticated numerical model of seismic wave propagation in a 3-D medium.

3.3 Energy partitioning among P, SV, and SH waves

Teleseismic P, SV, and SH waves are relatively rich in information about the source because they are less prone to scattering despite their smaller amplitudes. As pointed

out above, backprojection that utilizes teleseismic P-waves of secondary microseisms has superior spatial resolution and localization capability because scattering in the mantle is weaker than the scattering of surface waves in the crust. Energy partitioning is also more easily observable for characterization of the source because this energy partitioning more directly reflects source characteristics.

First, let us consider the energy partitioning of secondary microseisms with frequencies above 0.1 Hz. In this frequency range, recent observations of P, SV, and SH waves show MS amplitudes of P-wave amplitudes that are an order of magnitude larger than the SV waves.[84),85)] For example, Nishida and Takagi (2016) estimated the ratio between teleseismic P- and S-waves of secondary microseisms excited under the Atlantic Ocean[85)] using the Japanese array. Figure 5 shows clear P-, SV- and SH-wave propagation in the secondary microseismic band.[85)] The observed amplitudes suggest that pressure sources at the surface of the ocean can explain the observed amplitude ratios. Observed SV waves could be explained by P–SV conversion at the seafloor.[118)] The observed P waves can be modeled using ray-theoretical Green's functions with source site effects caused by water reverberations.[118),150)] Because the source area of the secondary microseisms for severe storms tend to be localized, they can be approximated by a vertical single force at the centroid location[85)] (see also subsections 2.2 and 4.3). Figure 8 shows the centroid locations with corresponding single forces for a rapidly deepening cyclonic low-pressure area known as a "weather bomb" over the Atlantic Ocean. The amplitude, on the order of 10^{11} N, can be explained quantitatively by an ocean wave action model (WAVEWATCH III[151)]). The order is also consistent with an equivalent single force of a severe storm estimated by a past study.[120)]

The detection of body waves with frequencies below 0.1 Hz is more challenging because of weaker amplitudes, particularly in the frequency ranges of seismic hum and primary microseisms.[121),123),152)] Although the weaker amplitude makes it difficult to infer the source locations using the backprojection method, the global average of the energy partitioning is also informative. In this frequency range, the radial–radial component (RR) and vertical–vertical (ZZ) components of shear-coupled PL waves are dominant, and weaker phases such as P, PKP, PcP, and SH[123)] can also be detected in the spatio-temporal domain. Figure 6 shows these features in the FK domain. This figure shows that the observed body-wave amplitudes are consistent with the synthetic FK spectra based on shear traction on the Earth's surface. These results support the inference that the force system can be characterized by random shear traction on the seafloor.

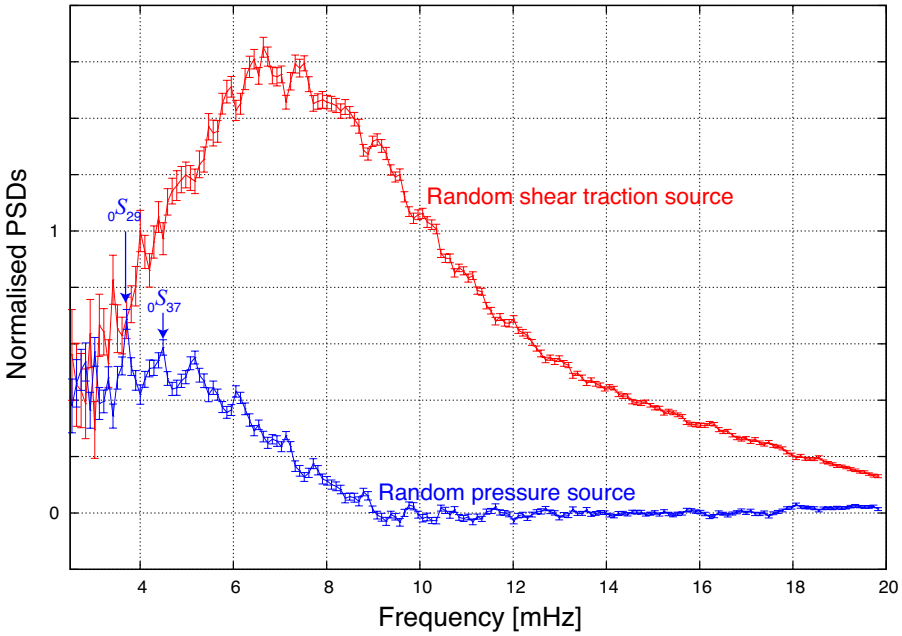

Figure 8: Power spectra of the effective pressure (blue line) and the effective shear traction (red line) normalized according to the reference model with bootstrap errors. Power spectra of the effective pressure and shear traction are defined by the corresponding power spectrum per unit wavenumber. The power spectrum of the effective pressure shows two local maxima, at 3.7 and 4.4 mHz, which correspond to acoustic coupling modes ($_0S_{29}$, $_0S_{37}$, respectively) between the fundamental spheroidal and atmospheric acoustic modes. From Nishida (2014).[121)]

4 Excitation mechanisms

All of the observed source distribution of the ambient seismic wave field show that the dominant source is oceanic wave activity. To evaluate the physical excitation mechanisms by this activity, it is essential to determine whether the sources are coastal or pelagic. The energy partitioning summarized in the previous section elucidates the equivalent force system, which can be characterized by a linear or second-order responses to oceanic waves depending on the typical frequency of those waves. Based on the observations, the physical excitation mechanisms associated with typical frequencies, i.e., seismic hum, primary microseisms and secondary microseisms, are discussed below. We also discuss a possible secondary contribution of atmospheric disturbances to seismic hum.

4.1 Seismic hum

At the first stage of these studies, atmospheric disturbances were recognized as the major excitation sources[40),50),60),61)] as described in section 1. Watada and Masters (2001) pointed that ocean infragravity waves excite seismic hum based on observation of ocean bottom pressure gauge.[153)] Comparisons of estimated source distribution[69),70),72),92)] with ocean wave height model showed that the dominant sources are ocean infragravity waves. The energy partitioning between the toroidal and spheroidal modes suggests that the source is represented by random shear traction at the seafloor. To clarify the force system quantitatively, source spectra of the random pressure and shear traction on Earth's surface were inferred by fitting synthetic spectra to observed cross-spectra between pairs of 618 global broadband stations,[121)] as shown in Figure 8. The result indicates dominance of shear-traction for frequencies above 5 mHz. However, pressure sources at the seafloor become important for frequencies below 5 mHz. Physical mechanisms other than the topographic coupling of ocean infragravity waves must also be considered.

Shear traction can be attributed to the topographic coupling between ocean infragravity waves and background Love and Rayleigh waves.[13),14),143)] Here we consider a simplified model of the topographic coupling shown in Figure 9. First, a wave packet of ocean infragravity waves propagates. Incremental pressure δp exerted by the ocean infragravity wave $\rho g \zeta$ acts on the seafloor, where ρ is the water density, g is gravitational acceleration, and ζ is vertical displacement of the sea surface (Figure 9(a)). The pressure fluctuation propagates to the right in Figure 9 with phase velocity of $\sqrt{gD}$, where D is water depth. In the case of a flat seafloor, the net incremental pressure acting on the seafloor is canceled out (Figure 9 (a)). When a seamount exists beneath the wave packet, the horizontal component of the net incremental traction force remains. The net horizontal force exerted on the

seamount excites seismic surface waves. This coupling occurs efficiently when the wavelength λ of the infragravity waves at the frequency and the horizontal scale of the seamount match.

To estimate this coupling more realistically, the statistical distribution of hills is introduced (Figure 10). Then, the excitation of seismic waves by the topographic coupling can be characterized by two stochastic parameters: the equivalent surface shear traction $\tau(f)$, and the correlation length $L_s(f)$. These values can be estimated as follows:

$$\tau(f) \sim p(f) C \frac{H(\lambda)^2}{\lambda^2}, L_s(f) \sim \lambda = \frac{\sqrt{gD}}{f}, \tag{1}$$

where $H(\lambda)$ is the height of the hill with a horizontal scale of the wavelength λ, C is a nondimensional statistical parameter of the hill's distribution,[11),13)] and p is the power spectrum of pressure at the seafloor with an order of magnitude of 10^4 $\mathrm{Pa^2 Hz^{-1}}$.[154)–156)] These two parameters can explain the observations despite the high uncertainty. These two parameters cannot be constrained independently from the observations. They can only be inferred in combination, which reflects forcing per unit wavenumber (effective shear traction[121)]) given by

$$\tau(f) \frac{L_s(f)^2}{4\pi R^2}. \tag{2}$$

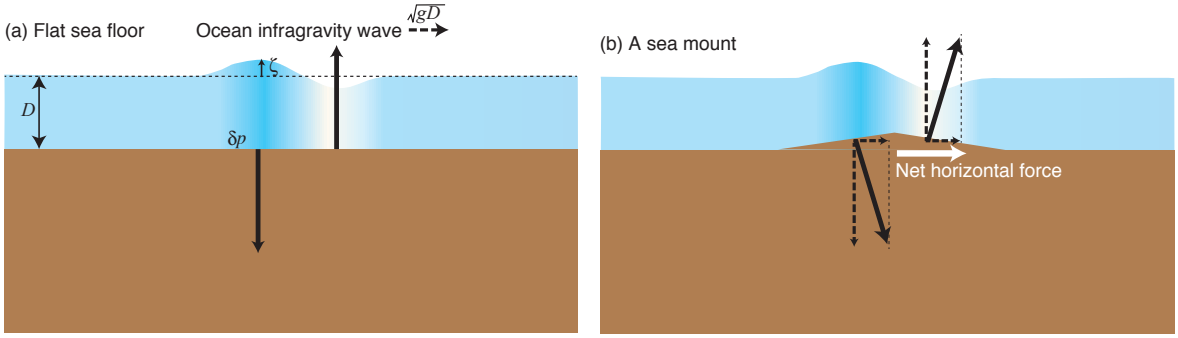

Figure 9: Schematic of the topographic coupling between ocean infragravity waves and seismic surface waves. (a) A wave packet of ocean infragravity wave propagates with phase velocity of $\sqrt{gD}$ to the right. In this case, because the seafloor is flat, the net incremental pressure δp acting on the seafloor by the ocean infragravity wave is canceled out. (b) A seamount exists beneath the wave packet. The vertical component of the net incremental traction force is canceled out. However, the horizontal component remains and excites seismic surface waves.

Ocean infragravity waves are generated by nonlinear forcing caused by higher-frequency wind waves with dominant periods of approximately 10 s in the surf zone.[157)–159)] When two wind wave trains travel in opposite directions, ocean infragravity waves are generated based on the difference in frequency between these waves. Ocean infragravity waves are trapped in the shallow water (low-velocity re-

gions) where strong nonlinear forcing occurs,[160] known as edge waves. In the shallow waters of the surf zone, the fronts of infragravity waves steepen and increase in amplitude; this phenomenon is known as surf beat. Some portion of the energy leaks into the deep ocean (leaky waves). Array analysis of ocean-floor pressure gauges in the deep sea record such propagation from coasts exposed by storms.[154),161),162] These leaky waves can travel across oceans with typical durations of several days.[163] The typical amplitudes observed for leaky waves are 5–10 mm,[164] although these amplitudes show seasonal variations. The ocean wave action model has thus been extended from wind waves to ocean infragravity waves,[165] and can capture between 30% and 80% of the variance in the heights of these waves, although they are not yet fully understood.

To explain the observed effective pressure source below 5 mHz, there are now two possible origins: ocean waves and atmospheric disturbances.

First, let us consider the linear and nonlinear excitation mechanisms of ocean waves. When ocean infragravity waves are generated, a similar forcing of Rayleigh waves at the difference in frequency can be anticipated.[155),166] However, the amplitude of these waves is estimated to be negligible.[10),113),167] The next mechanism is linear forcing caused by the pressure fluctuations modulated by a sloping seafloor in coastal regions where the typical spatial scale is longer than the wavelength of the ocean infragravity waves.[113] This mechanism can explain the observed amplitudes within the uncertainty of the parameters.[113]

Another possible source is atmospheric disturbances. Observed clues for this mechanism are (1) coupling between the fundamental spheroidal modes of the Earth and atmospheric acoustic modes,[54),168] and (2) the background atmospheric Lamb waves.[125] Here, atmospheric Lamb wave propagates non-dispersively in the horizontal direction with a sound velocity of about 310 $\mathrm{m\,s^{-1}}$, while it is balanced hydrostatically in the vertical direction.[169] The observed coupling characterized by excess amplitudes of two slightly different resonant peaks at 3.7 and 4.4 mHz suggests that the excitation sources have a little energy in the atmosphere. The observed Lamb waves suggest that their common excitation sources for the coupled modes and the Lamb waves are atmospheric disturbances in the troposphere.[125] The atmospheric disturbances in the troposphere are also expected to contribute to the excitation of the other uncoupled fundamental spheroidal modes. A schematic of atmospheric excitation by cumulus convection in the troposphere[170] specifically is illustrated in Figure 10. The power spectrum of random atmospheric pressure fluctuations p from cumulus convection with the correlation length L_p may contribute the observed pressure source of seismic hum below 8 mHz (Figure 8). Because these parameters are associated with high uncertainties, observational constraints on the global averages of these parameters are required. For the further discussions, the

source locations should be addressed.

4.2 Primary microseisms

With increasing frequency, pressure fluctuation of ocean gravity waves cannot reach the seafloor in the deep ocean because these fluctuations decay exponentially according to the wavelength. At 0.07 Hz, the pressure of ocean gravity waves at the seafloor at a depth of 100 m is about 1% of the surface pressure. As a result, the observed coastal source distribution of primary microseisms can be explained by excitation by ocean gravity waves at the seafloor in coastal areas[10),113),171),172)] shallower than approximately 100 m. Although pressure fluctuations of ocean gravity waves cannot excite seismic waves in a stratified Earth, the pressure fluctuations modulated by a sloping seafloor at the shore can excite them.[113),173),174)] However, this model cannot explain the observed equipartition between Love and Rayleigh waves.[14),68)] This energy partition suggests excitations by shear traction at the seafloor, which may also explain the little observation of teleseismic P waves of primary microseisms caused by the radiation pattern of these waves.[123)] A possible physical mechanism is linear topographic coupling at the shallow seafloor,[13),143)] as shown in Figure 10(b). Observations from a seismic array in Europe show that the energy ratio of Love to Rayleigh waves depends on location.[100)] This observation may be attributed to radiation patterns controlled by bathymetry. To further understanding of these observations, more quantitative modeling of this wave excitation with realistic topography should be carried out.

This mechanism requires a linear relationship between ocean wave height and the excited seismic wave amplitude. This relationship was confirmed through comparison with ocean wave height data collected by buoys. When a severe storm occurs, the evolution of the peak frequency of primary microseisms over time coincides with that of ocean wave height data.[10),173),175)] Figure 11 shows an observational comparison with running spectra of ocean wave heights and of ground motion at the seafloor during times of high local ocean wave activity. The excitation amplitude of primary microseisms should be linearly proportional to significant ocean wave height when the dominant excitation source is near the station.[171)]

The major difficulty for source localizations is scattering by the water column and thick sediment. To avoid this difficulty, source localization by teleseismic body wave microseisms may be applicable to constrain the excitation, as in secondary microseisms. However, the teleseismic body-wave amplitudes are too small for source localization.[123)] The recent development of dense arrays may make this localization possible. For source localization, tidal modulation of primary microseisms[176)] may also be applicable as a proxy for the coastal generation because of the strong non-

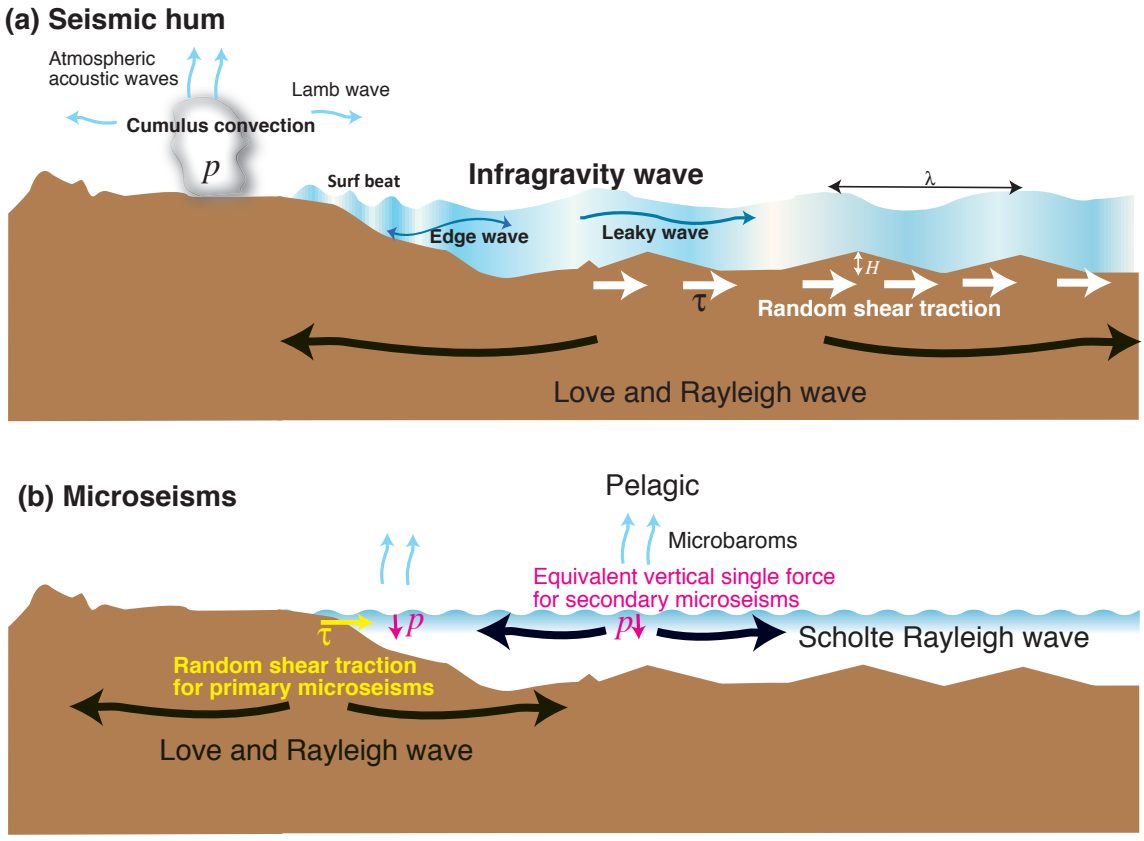

Figure 10: (a) Schematic of the excitation mechanisms of seismic hum. The observed equivalent shear traction source at the seafloor can be explained by the topographic coupling between ocean infragravity waves and the background Love and Rayleigh waves. This coupling occurs efficiently when the wavelength λ of the infragravity waves at the corresponding frequency and the horizontal scale of the topography match each other. $H(\lambda)$ is the height of the hill with a horizontal scale of λ. This figure also shows a schematic of the atmospheric excitation caused by cumulus convection in the troposphere. Random pressure fluctuation of cumulus convection δp with the correlation length L_p excites background Rayleigh waves. (b) Schematic of excitation mechanisms of primary and secondary microseisms. The excitation of primary microseisms can be explained by the topographic coupling in a shallow coastal region. The excitation mechanism of secondary microseisms can be explained by nonlinear forcing at the surface of the ocean by ocean swell in both coastal and pelagic areas. When two regular wave trains traveling in opposite directions with displacement amplitudes at the sea surface interact, the second-order pressure fluctuation δp at the sea surface with the correlation length L_p excites background Rayleigh waves.

linear effect between ocean gravity waves and tides in shallow source areas caused by the tidal modulation of ocean infragravity waves.[177)–179)]

4.3 Secondary microseisms

Observed source distributions indicate that the excitation sources are ocean swell activities. Figure 11 shows that the frequency of secondary microseisms is double that of the ocean swell. This relation is confirmed by the observation of a severe distant storm event,[10),173),175)] and can be explained by the Longuet-Higgins mechanism.[20)]

First, let us consider an analogy of a pendulum[181)] proposed by Longuet-Higgins (1953) illustrated in lower panels of Figure 12 (a)–(d). This analogy applies to two regular wave trains traveling in opposite directions with a displacement amplitude at the sea surface that interact as shown in Figure 12. The upper panels of this figure show a standing wave at angular frequency ω, that does not propagate toward a specific direction. Here we consider a standing wave with the displacement amplitudes of sea surface ζ given by

$$\zeta = \zeta_0 \cos kx \cos \omega t, \tag{3}$$

where ω is angular frequency, k is wavenumber, ζ_0 is the amplitude, x is horizontal location, and t is time. The center of mass oscillates vertically with frequency 2ω; the centroid depths of Figure 12(a) and (c) are higher than those of (b) and (d). To cause the periodic vertical oscillations, a periodic external force with frequency 2ω is required; the pendulum depicted in the lower panels may be a suitable analog. Displacement of the pendulum corresponds to movement of water and the force at the pivot point represents pressure at the bottom. The bottom pressure is estimated to be

$$-\rho(\zeta_0\omega)^2 \frac{\cos(2\omega t)}{2} \tag{4}$$

as shown in Figure 12(e). The second-order pressure fluctuations reach the deep ocean floor, whereas pressure fluctuation of linear ocean gravity waves attenuates exponentially,[182)] as shown by ocean floor observations (Figure 11(c)). Thus, pressure fluctuations, which correspond to forcing at the pivot point, should be proportional to the power of the amplitudes of ocean swell.

Hasselmann (1963) extended the Longuet-Higgins theory to random wave fields.[10)] For quantitative assessment, let us summarize the theory of the relationship between second-order forcing by ocean swell and the frequency–directional spectrum of ocean swell[183)] as described by Ardhuin and Herbers (2013). The power spectrum of the second-order pressure fluctuation F_p at frequency f with the correlation length $L_p(f)$

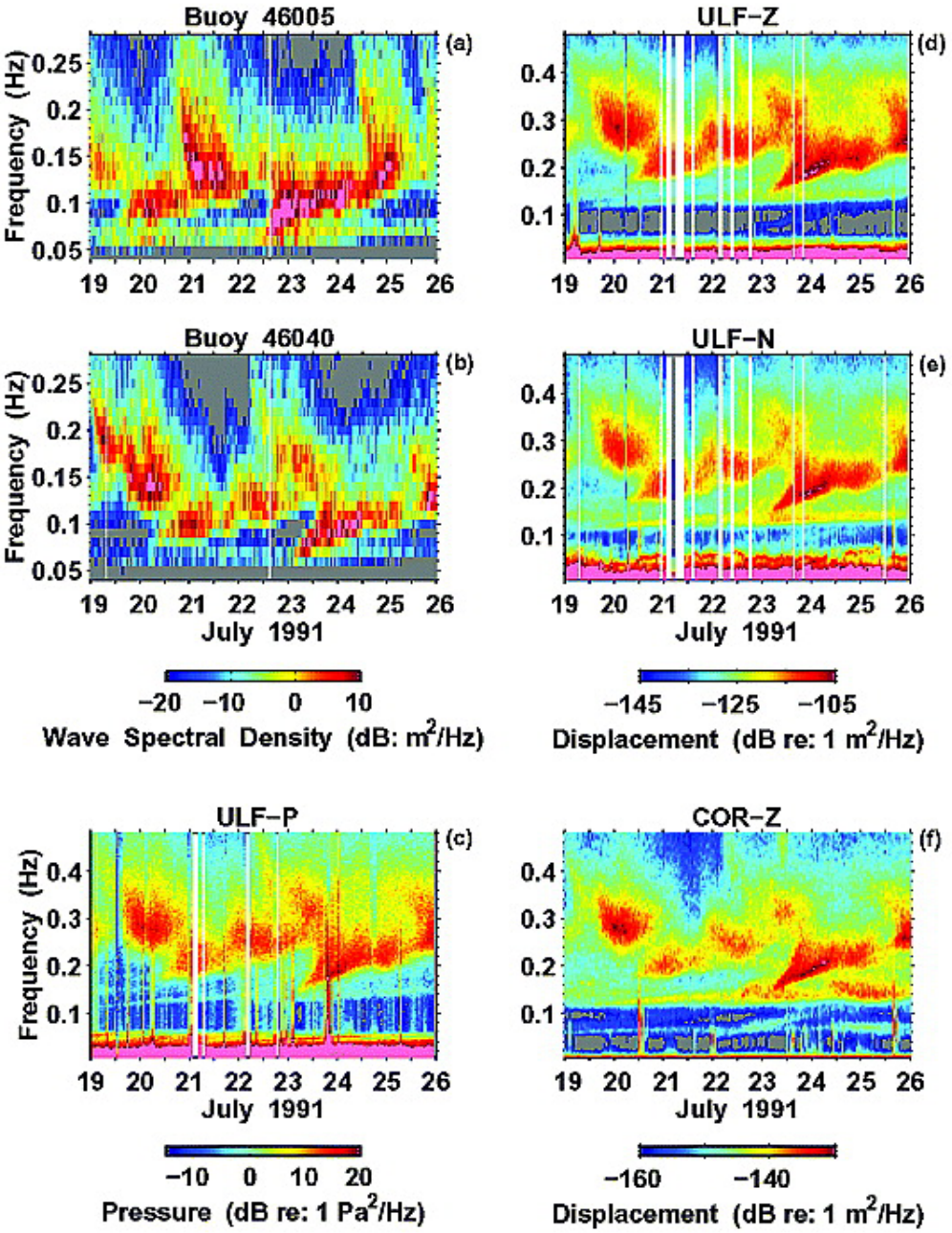

Figure 11: Wave spectral variation during the July 1991 ULF/VLF (ULF, ultra-low frequency; VLF, very low frequency) experiment along the Oregon coast. (a) Running spectrum of wave height data at an offshore the National Oceanic and Atmospheric Administration (NOAA) buoy 46005. (b) Running spectrum at a nearshore NOAA buoy 46040. Ocean bottom power spectra at a coastal ocean floor seismic station at ULF from the (c) differential pressure gauge, ULF-P, (d) vertical seismometer, ULF-Z, and the (e) northerly-oriented horizontal component seismometer, ULF-N, for the same time periods as the wave data. (f) The corresponding displacement response at the inland seismometer COR. All spectra are in dB, with spectral values outside the ranges shown set equal to their respective boundaries, with the highest amplitudes in pink. Figures 11a and 11b and Figures 11d and 11e have the same spectral ranges. Temporal tick marks indicate 12-hour intervals. From Figure 6 of Bromirski (2002).[180)]

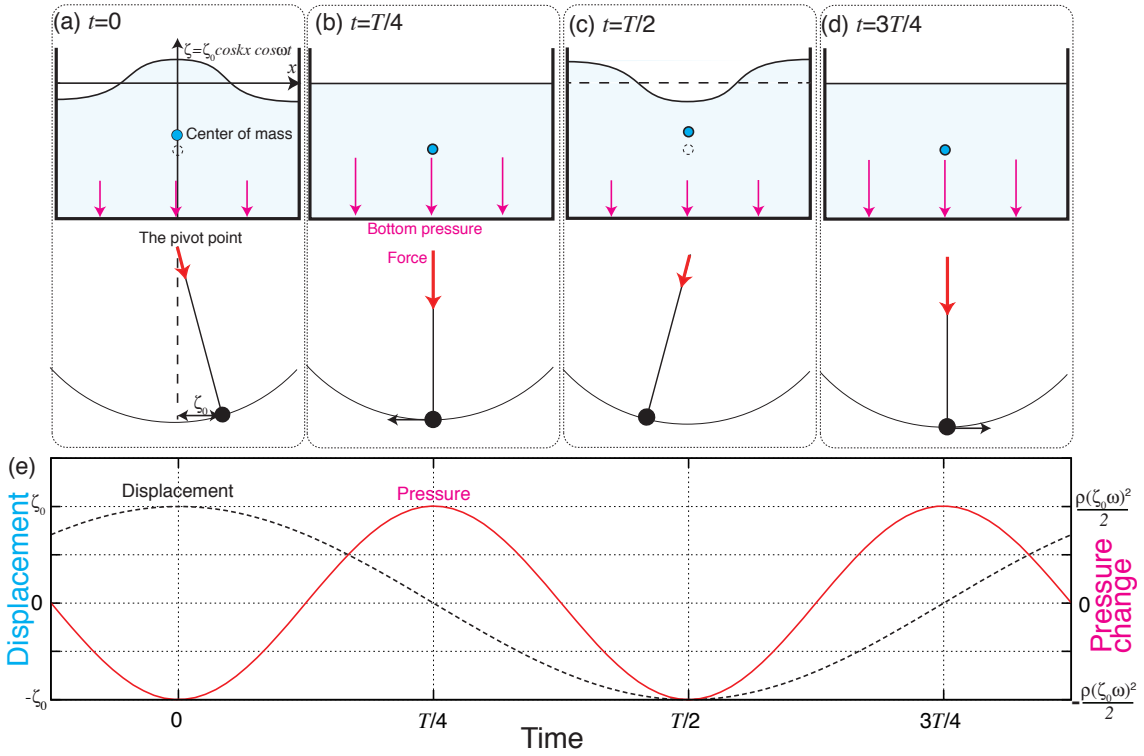

Figure 12: (a)–(d): Snapshots of a simplified model analogous to a pendulum. A standing wave that does not propagate toward a specific direction. Here T is the period given by $2\pi/\omega$. (e): Displacement of the mass and the force at the pivot point against time. This figure is illustrated after Longuet-Higgins (1953).[181)]

can be represented by a frequency–directional spectrum of ocean waves:

$$F_p(\boldsymbol{k} \sim 0, f) = \left(\frac{2\pi}{L}\right)^2 \rho^2 g^2 f E^2(f/2) I(f/2), \tag{5}$$

where ρ is the density of water, g is the gravitational acceleration, f is the frequency of secondary microseisms, $E(f/2)$ is the power spectrum of ocean wave height, and $I(f/2)$ is the directional overlap integral, which shows the contribution of the standing wave component. If the source area S is localized, the MS amplitude of the centroid single force can be expressed[10),85),112)] as

$$2\pi\sqrt{\left(\int F_p(f)df\right) S}. \tag{6}$$

Based on this framework, the amplitude of the secondary microseism A_2 is proportional to the power of ocean wave height in the dominant source area, whereas that of the primary microseisms A_1 is proportional to ocean wave height in the dominant source area. At coastal stations, because common sources for both primary and secondary microseisms are anticipated to be located near stations, A_2 is expected to be proportional to $(A_1)^2$. Figure 13(a) provides an example of this phenomenon

in Japan. This figure is a plot of probability density against MS amplitudes of A_1 and those of A_2, which show this relationship clearly. In contrast, at continental stations in China, both wavefields of primary and secondary microseisms are more stationary (Figure 13(b)), because they are scattered during the propagations from the distant sources distributed on larger areas.

Recent research has demonstrated that the Longuet-Higgins mechanism, in conjunction with an ocean wave action model, can quantitatively represent observed Rayleigh waves,[26),111),113)] including those from pelagic and coastal sources. Source site effects caused by the water column are also crucial for quantitative comparison. Resonance in the water column amplifies secondary microseisms depending on the water depth at the source area.[26),118)] Although Rayleigh wave propagation from ocean to continent is complex,[75)] the simple 1-D Earth model can explain most of the observed amplitudes. This theory can now explain the observed amplitudes of teleseismic P-wave microseisms[81),85),114),118),150)] (Figure 3 and 4). These figures show that observed teleseismic P-wave microseisms can generally be explained by the Longuet-Higgins–Hasselmann theory. The theory with an ocean wave action model can predict source locations inferred from P-wave microseisms.[81),85),114),118),150)] Local environmental conditions, which are not considered in the ocean wave action model, also contribute to excitation. For example, the presence of sea ice around stations[111)] and local winds[110)] are correlated with the local activity of secondary microseisms. Discrepancies between seismic observation and the ocean wave action model may contribute to constructing a better ocean wave action model.

5 Conclusions

The ambient seismic wave field is excited by oceanic gravity waves primarily between 1 mHz and 1 Hz. Based on the typical frequencies of these waves, they are categorized into seismic hum (1–20 mHz), primary microseisms (0.02–0.1 Hz), and secondary microseisms (0.1–1 Hz).

Seismic hum has been observed globally at a number of stations. The excited modes of these oscillations are almost exclusively fundamental spheroidal and toroidal modes. The amplitudes of the toroidal modes are larger than those of the spheroidal modes. The inferred spatio-temporal variations of source distribution suggest that ocean infragravity waves are the dominant source of these oscillations. The source of this excitation may be random shear traction at the seafloor. This shear traction can be explained by linear topographic coupling between ocean infragravity waves and seismic modes. The pressure source is also significant for oscillations below 5 mHz. In this frequency range, the power spectra of vertical ground motions show two resonant peaks, at 3.7 and 4.4 mHz, which show acoustic

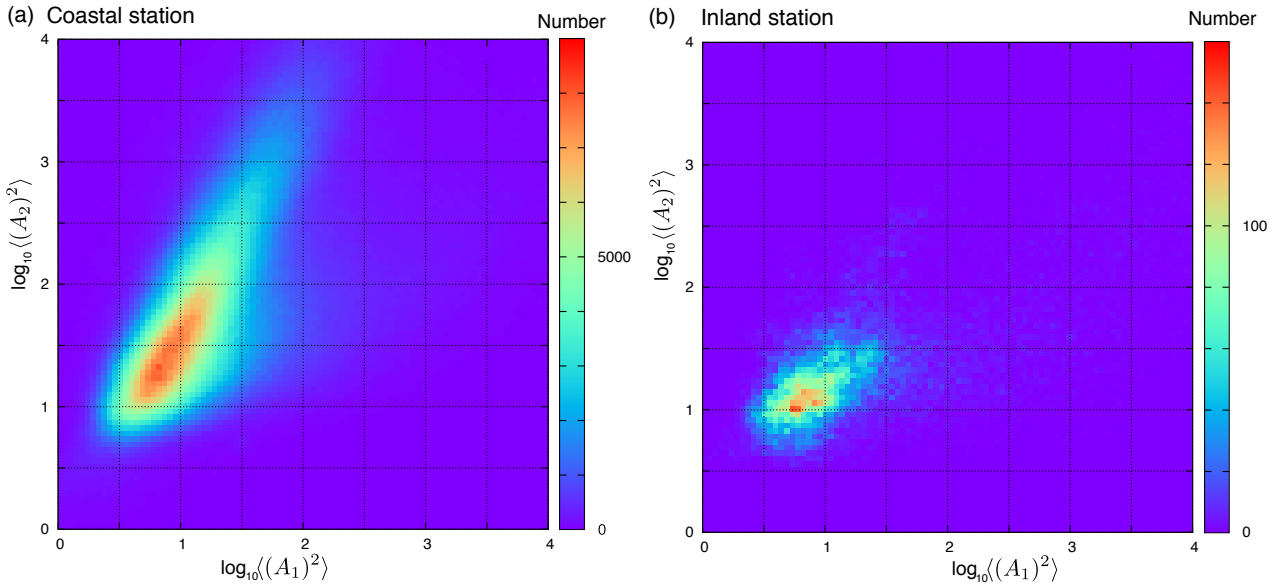

Figure 13: (a) Plot of probability density against MS amplitudes of primary microseisms from 0.05 to 0.1 Hz $\langle(A_1)^2\rangle$ and those of secondary microseisms from 0.1 to 0.2 Hz $\langle(A_2)^2\rangle$ for vertical components at all F-net broadband stations in Japan deployed by the National Research Institute for Earth Science and Disaster Resilience from 2004 to 2010. Values are normalized based on the New Low Noise Model (NLNM).[12] The value of $\langle(A_2)^2\rangle$ is approximately proportional to $\langle(A_1)^2\rangle^2$. (2) The probability density plot for vertical components at inland Chinese stations LSA, HIA, and WMQ deployed by the New China Digital Seismograph Network from 2004 to 2005. This figure suggests that the seismic wave field could be more diffusive.

resonance between the atmosphere and the solid Earth. Background atmospheric Lamb waves are also observed in this frequency range. These observations suggest that atmospheric disturbance, such as cumulus convection, may also contribute to excitation below 5 mHz.

The excitation sources of primary microseisms are distributed in shallow coastal areas. This excitation can be explained by forcing by ocean swell at shallow depths on continental shelves. Equipartition of Love and Rayleigh wave energy suggests that linear topographic coupling of ocean swell with Love and Rayleigh waves at the shallow depths plays an important role in these excitations.

The excitation sources of secondary microseisms are distributed in both shallow, coastal areas and pelagic areas. Recent developments in source location with body-wave microseisms enable us to estimate forcing quantitatively. Inferred spatio-temporal variations of source distribution show that these microseisms can be explained by nonlinear forcing caused by standing ocean swell at the sea surface. An ocean wave action model can, therefore, be used to predict excitation amplitudes. Quantitative comparison of forcing estimated using an ocean wave action model with forcing inferred from seismic records may clarify ocean wave activities.

For a comprehensive understanding of the ambient seismic wave field, the solid Earth, the ocean, and the atmosphere must be considered as a coupled system.

Acknowledgments

I thank my collaborators in these studies. In particular, I appreciate Yoshio Fukao and Naoki Shibata for long-term collaboration and support. I thank two anonymous reviewers and the Editor Yoshio Fukao for their constructive comments and suggestions. This research was partially supported by JSPS KAKENHI Grant Numbers JP26400448. I am grateful to numerous of people associated with the Incorporated Research Institutions for Seismology (IRIS), the Observatories & Research Facilities for European Seismology (ORFEUS), and the National Research Institute for Earth Science and Disaster Resilience (NIED) for maintaining these networks and making the data readily available. Maps were generated using the generic mapping tools (GMT) software package.

References

1) Bertelli, T. (1872) Osservazioni sui piccoli movimenti dei pendoli. Bull. Meteorol. dell'Osservatorio dell Coll. Rom. Roma, Italy **101**, 20pp.

2) Meltzer, A., Rudnick, R., Zeitler, P., Levander, A., Humphreys, G., Karlstrom, K., Ekström, G., Carlson, R., Dixon, T., Gurnis, M., Shearer, P., Van Der Hilst, R. (1999) USArray initiative. GSA Today **9**, 8–10.

3) Okada, Y., Kasahara, K., Hori, S., Obara, K., Sekiguchi, S., H. Fujiwara, Yamamoto, A. (2004) Recent progress of seismic observation networks inJapan: Hi-net, F-net, K-net, KiK-net. Earth Planets Space **56**, xv–xviii.

4) Snieder, R., Larose, E. (2013) Extracting Earth's Elastic Wave Response from Noise Measurements. Annu. Rev. Earth Planet. Sci. **41**, 183–206.

5) Snieder, R. (2004) Extracting the Green's function from the correlation of coda waves: A derivation based on stationary phase. Phys. Rev. E **69**, 046610.

6) Tsai, V. C. (2009) On establishing the accuracy of noise tomography traveltime measurements in a realistic medium. Geophys. J. Int. **178**, 1555–1564.

7) Weaver, R., Froment, B., Campillo, M. (2009) On the correlation of non-isotropically distributed ballistic scalar diffuse waves. J. Acoust. Soc. Am. **126**, 1817–1826.

8) Froment, B., Campillo, M., Roux, P., Gouédard, P., Verdel, A., Weaver, R. L. (2010) Estimation of the effect of nonisotropically distributed energy on the apparent arrival time in correlations. GEOPHYSICS **75**, SA85-SA93.

9) Bonnefoy-Claudet, S., Cotton, F., Bard, P.-Y. (2006) The nature of noise wavefield and its applications for site effects studies: A literature review. Earth-Science Reviews **79**, 205–227.

10) Hasselmann, K. (1963) A statistical analysis of the generation of microseisms. Rev. Geophys. **1**, 177-210.

11) Nishida, K. (2013) Earth's Background Free Oscillations. Annu. Rev. Earth Planet. Sci. **41**, 719–740.

12) Peterson, J. (1993) OBSERVATIONS AND MODELING OF SEISMIC BACKGROUND NOISE. U.S. Geol. Surv. Open File Rep. **93-322**, 1.

13) Fukao, Y., Nishida, K., Kobayashi, N. (2010) Seafloor topography, ocean infragravity waves, and background Love and Rayleigh waves. J. Geophys. Res. **115**, B04302.

14) Nishida, K., Kawakatsu, H., Fukao, Y., Obara, K. (2008) Background Love and Rayleigh waves simultaneously generated at the Pacific Ocean floors. Geophys. Res. Lett. **35**, L16307.

15) Bernard, P. (1990) Historical sketch of microseisms from past to future. Phys. Earth Planet. Inter. **63**, 145–150.

16) Omori, F. (1905) Horizontal pendulum diagram obtained during a storm. Bull. Imperial Earthq. Inv. Comm. **21**, 5–8.

17) Gutenberg, B. (1931) Microseims in north america. Bull. Seismol. Soc. Am. **21**, 1–24.

18) Gherzi, E. (1945) Trembling Earth. The XX century **8**, 251–254.

19) Sezawa, K., Kanai, K. (1939) Microseisms caused by transmission of atmospheric distrubances. II. Bull. Earthq. Res. Inst. **17**, 548–558.

20) Longuet-Higgins, M. S. (1950) A Theory of the Origin of Microseisms. Proc. R. Soc. A **243**, 1–35.

21) Wiechert, E. (1904) Discussion, Verhandlung der zweiten Internationalen Seismologischen Konferenz. Beitrage zur Geophysik **2**, 41–43.

22) Omori, F. (1909) Report on the observation of pulsatory oscillations in japan 1st paper. Bull. Imperial Earthq. Inv. Comm. **3**, 1–35.

23) Omori, F. (1911) Report on the observation of pulsatory oscillations in japan 2nd paper. Bull. Imperial Earthq. Inv. Comm. pp. 109–137.

24) Omori, F. (1918) On a relation between microseisms and ocean swell (in japanese). Rep. Imperial Earthq. Inv. Comm. **89**, 12–18.

25) Miche, A. (1944) Mouvements ondulatoires de la mer en profondeur croissante ou décroissante. Première partie. Mouvements ondulatoires périodiques et cylindriques en profondeur constante. Annales des Ponts et Chaussées **114**, 42–78.

26) Kedar, S., Longuet-Higgins, M., Webb, F., Graham, N., Clayton, R., Jones, C. (2008) The origin of deep ocean microseisms in the North Atlantic Ocean. Proc. R. Soc. A **464**, 777–793.

27) Ardhuin, F., Stutzmann, E., Schimmel, M., Mangeney, A. (2011) Ocean wave sources of seismic noise. J. Geophys. Res. **116**, 1–21.

28) Donn, W. L., Posmentier, E. S. (1967) Infrasonic waves from the marine storm of April 7, 1966. J. Geophys. Res. **72**, 2053–2061.

29) Donn, W. L. (1967) Natural infrasound of five seconds period. Nature **215**, 1469–1470.

30) Donn, W. L., Naini, B. (1973) Sea wave origin of microbaroms and microseisms. J. Geophys. Res. **78**, 4482–4488.

31) Arendt, S., Fritts, D. C. (2000) Acoustic radiation by ocean surface waves. J. Fluid Mech. **415**, 1–21.

32) Benioff, H., Press, F., Smith, S. (1961) Excitation of the free oscillations of the Earth by earthquakes. J. Geophys. Res. **66**, 605–619.

33) Dahlen, F. A., Tromp, J. (1998) *Theoretical Global Seismology*, Princeton University Press, Princeton.

34) Thomson, W. (1863) On the Rigidity of the Earth. Philosophical Transactions of the Royal Society of London **153**, 573–582.

35) Benioff, H., Harrison, J. C., LaCoste, L., Munk, W. H., Slichter, L. B. (1959) Searching for the Earth's free oscillations. J. Geophys. Res. **64**, 1334–1337.

36) Kanamori, H. (1998) SEISMOLOGY: Enhanced: Shaking Without Quaking. Science **279**, 2063–2064.

37) Tanimoto, T. (2001) CONTINUOUS FREE O SCILLATIONS : Atmosphere-Solid Earth Coupling. Annu. Rev. Earth Planet. Sci. **29**, 563–584.

38) Christensen-Dalsgaard, J. (2002) Helioseismology. Rev. Mod. Phys. **74**, 1073–1129.

39) Kobayashi, N. (1996) Oscillations of solid planets excited by atmospheric random motions. *Fall Meet. Jpn. Soc. Planet. Sci.*, Fukuoka.

40) Kobayashi, N., Nishida, K. (1998) Continuous excitation of planetary free oscillations by atmospheric disturbances. Nature **395**, 357–360.

41) Lognonné, P. (2005) Planetary Seismology. Annu. Rev. Earth Planet. Sci. **33**, 571–604.

42) Nishida, K., Montagner, J.-P., Kawakatsu, H. (2009) Global surface wave tomography using seismic hum. Science **326**, 112.

43) Nawa, K., Suda, N., Fukao, Y., Sato, T., Aoyama, Y., Shibuya, K. (1998) Incessant excitation of the Earth's free oscillations. Earth Planets Space **50**, 3–8.

44) Nawa, K., Suda, N., Fukao, Y., Sato, T., Tamura, Y. (2000) Incessant excitation of the Earth's free oscillations: global comparison of superconducting gravimeter records. Phys. Earth Planet. Inter. **120**, 289–297.

45) Nawa, K. (2003) Sea level variation in seismic normal mode band observed with on-ice GPS and on-land SG at Syowa Station, Antarctica. Geophys. Res. Lett. **30**, 1–4.

46) Suda, N., Nawa, K., Fukao, Y. (1998) Earth's Background Free Oscillations. Science **279**, 2089–2091.

47) Tanimoto, T., Um, J., Nishida, K., Kobayashi, N. (1998) Earth's continuous oscillations observed on seismically quiet days. Geophys. Res. Lett. **25**, 1553–1556.

48) Widmer-Schnidrig, R. (2003) What Can Superconducting Gravimeters Contribute to Normal-Mode Seismology? Bull. Seismol. Soc. Am. **93**, 1370–1380.

49) Nishida, K., Kobayashi, N. (1999) Statistical features of Earth's continuous free oscillations. J. Geophys. Res. **104**, 28741–28.

50) Tanimoto, T., Um, J. (1999) Cause of continuous oscillations of the Earth. J. Geophys. Res. **104**, 28723–28739.

51) Agnew, D. C. D., Berger, J. O. N. (1978) Vertical seismic Noise at Very Low Frequencies. J. Geophys. Res. **83**, 5420–5424.

52) Gutenberg, B. (1912) Die seismische bodenunruhe (dissertation). Gerl. Beiträge z. Geophys. **11**, 314–353.

53) Gutenberg, B. (1921) *Untersuchungen über die Bodenunruhe mit perioden von 4s-10s in Europa*, Série B., Publications du Bureau central de l'association internationale de sismologie.

54) Nishida, K., Kobayashi, N., Fukao, Y. (2000) Resonant Oscillations Between the Solid Earth and the Atmosphere. Science **287**, 2244–2246.

55) Roult, G., Crawford, W. (2000) Analysis of ' background' free oscillations and how to improve resolution by subtracting the atmospheric pressure signal. Phys. Earth Planet. Inter. **121**, 325–338.

56) Kanamori, H., Mori, J. (1992) Harmonic excitation of mantle Rayleigh waves by the 1991 eruption of Mount Pinatubo, Philippines. Geophys. Res. Lett. **19**, 721–724.

57) Kanamori, H., Mori, J., Harkrider, D. G. (1994) Excitation of atmospheric oscillations by volcanic eruptions. J. Geophys. Res. **99**, 21947–21961.

58) Widmer, R., Zürn, W. (1992) Bichromatic excitation of long-period Rayleigh and air waves by the Mount Pinatubo and El Chichon volcanic eruptions. Geophys. Res. Lett. **19**, 765–768.

59) Watada, S., Kanamori, H. (2010) Acoustic resonant oscillations between the atmosphere and the solid earth during the 1991 Mt. Pinatubo eruption. J. Geophys. Res. **115**, 1–20.

60) Tanimoto, T. (1999) Excitation of normal modes by atmospheric turbulence: Source of long period seismic noise. Geophys. J. Int. **136**, 395–402.

61) Fukao, Y., Nishida, K., Suda, N., Nawa, K., Kobayashi, N. (2002) A theory of the Earth's background free oscillations. J. Geophys. Res. **107**, 2206.

62) Rost, S., Thomas, C. (2002) Array seismology: methods and applications. Rev. Geophys. **40**, 1008.

63) Ishii, M., Shearer, P. M., Houston, H., Vidale, J. E. (2005) Extent, duration and speed of the 2004 Sumatra–Andaman earthquake imaged by the Hi-Net array. Nature **435**, 933–936.

64) Schimmel, M., Stutzmann, E., Ardhuin, F., Gallart, J. (2011) Polarized Earth's ambient microseismic noise. Geochem. Geophys. Geosyst. **12**, n/a-n/a.

65) Schulte-Pelkum, V., Earle, P. S., Vernon, F. L. (2004) Strong directivity of ocean-generated seismic noise. Geochem. Geophys. Geosyst. **5**, 1–13.

66) Gal, M., Reading, A., Ellingsen, S., Koper, K., Burlacu, R., Gibbons, S. (2016) Deconvolution enhanced direction of arrival estimation using one- and three-component seismic arrays applied to ocean induced microseisms. Geophys. J. Int. **206**, 345–359.

67) Cessaro, R. (1994) Sources of primary and secondary microseisms. Bull. Seismol. Soc. Am. **84**, 142–148.

68) Friedrich, a., Krüger, F., Klinge, K. (1998) Ocean-generated microseismic noise located with the Gräfenberg array. J. Seismol. **2**, 47–64.

69) Rhie, J., Romanowicz, B. (2004) Excitation of Earth's continuous free oscillations by atmosphere-ocean-seafloor coupling. Nature **431**, 552–556.

70) Rhie, J., Romanowicz, B. (2006) A study of the relation between ocean storms and the Earth's hum. Geochem. Geophys. Geosyst. **7**, Q10004.

71) Kurrle, D., Widmer-Schnidrig, R. (2010) Excitation of long-period Rayleigh waves by large storms over the North Atlantic Ocean. Geophys. J. Int. **183**, 330–338.

72) Traer, J., Gerstoft, P., Bromirski, P. D., Shearer, P. M. (2012) Microseisms and hum from ocean surface gravity waves. J. Geophys. Res. **117**, B11307.

73) Shapiro, N. M., Campillo, M., Singh, S. K., Pacheco, J. (1998) Seismic channel waves in the accretionary prism of the Middle America Trench. Geophys. Res. Lett. **25**, 101–104.

74) Weaver, R. L., Lobkis, O. I. (2004) Diffuse fields in open systems and the emergence of the Green's function (L). J. Acoust. Soc. Am. **116**, 2731–2734.

75) Bromirski, P. D., Stephen, R. A., Gerstoft, P. (2013) Are deep-ocean-generated surface-wave microseisms observed on land? J. Geophys. Res. **118**, 3610–3629.

76) Gualtieri, L., Stutzmann, E., Capdeville, Y., Farra, V., Mangeney, A., Morelli, A. (2015) On the shaping factors of the secondary microseismic wavefield. J. Geophys. Res. **120**, 6241–6262.

77) Ishii, M., Shearer, P. M., Houston, H., Vidale, J. E. (2007) Teleseismic P wave imaging of the 26 December 2004 Sumatra-Andaman and 28 March 2005 Sumatra earthquake ruptures using the Hi-net array. J. Geophys. Res. **112**, B11307.

78) Gerstoft, P., Shearer, P. M., Harmon, N., Zhang, J. (2008) Global P, PP, and PKP wave microseisms observed from distant storms. Geophys. Res. Lett. **35**, 4–9.

79) Zhang, J., Gerstoft, P., Bromirski, P. D. (2010) Pelagic and coastal sources of P -wave microseisms: Generation under tropical cyclones. Geophys. Res. Lett. **37**, 1–6.

80) Zhang, J., Gerstoft, P., Shearer, P. M. (2010) Resolving P-wave travel-time anomalies using seismic array observations of oceanic storms. Earth and Planet. Sci. Lett. **292**, 419–427.

81) Hillers, G., Graham, N., Campillo, M., Kedar, S., Landès, M., Shapiro, N. (2012) Global oceanic microseism sources as seen by seismic arrays and predicted by wave action models. Geochem. Geophys. Geosyst. **13**.

82) Hillers, G., Campillo, M., Ma, K. F. (2014) Seismic velocity variations at TCDP are controlled by MJO driven precipitation pattern and high fluid discharge properties. Earth Planet. Sci. Lett. **391**, 121–127.

83) Obrebski, M., Ardhuin, F., Stutzmann, E., Schimmel, M. (2013) Detection of microseismic compressional (P) body waves aided by numerical modeling of oceanic noise sources. J. Geophys. Res. **118**, 4312–4324.

84) Liu, Q., Koper, K. D., Burlacu, R., Ni, S., Wang, F., Zou, C., Wei, Y., Gal, M., Reading, A. M. (2016) Source locations of teleseismic P, SV, and SH waves observed in microseisms recorded by a large aperture seismic array in China. Earth Planet. Sci. Lett. **449**, 39–47.

85) Nishida, K., Takagi, R. (2016) Teleseismic S wave microseisms. Science **353**, 919–921.

86) Randall, M. (1971) Elastic multipole theory and seismic moment. Bulletin of the Seismological Society of America **61**, 1321–1326.

87) Cox, H. (1973) Spatial correlation in arbitrary noise fields with application to ambient sea noise. J. Acoust. Soc. Am. **54**, 1289–1301.

88) Harmon, N., Rychert, C., Gerstoft, P. (2010) Distribution of noise sources for seismic interferometry. Geophys. J. Int. **183**, 1470–1484.

89) Nishida, K., Fukao, Y. (2007) Source distribution of Earth's background free oscillations. J. Geophys. Res. **112**, B06306.

90) Hanasoge, S. M. (2013) Measurements and kernels for source-structure inversions in noise tomography. Geophys. J. Int. **196**, 971–985.

91) Kurrle, D., Widmer-Schnidrig, R. (2006) Spatiotemporal features of the Earth's background oscillations observed in central Europe. Geophys. Res. Lett. **33**, 2–5.

92) Bromirski, P. D., Gerstoft, P. (2009) Dominant source regions of the Earth's "hum" are coastal. Geophys. Res. Lett. **36**, L13303.

93) Ermert, L., Villaseñor, A., Fichtner, A., Villase, A., Fichtner, A. (2016) Cross-correlation imaging of ambient noise sources. Geophys. J. Int. **204**, 347–364.

94) Stehly, L., Campillo, M., Shapiro, N. M. (2006) A study of the seismic noise from its long-range correlation properties. J. Geophys. Res. **111**, 1–12.

95) Agnew, D. C., Berger, J., Farrell, W. E., Gilbert, J. F., Masters, G., Miller, D. (1986) Project IDA: A decade in review. Eos **67**, 203–212.

96) Beauduin, R., Lognonné, P., Montagner, J. P., Cacho, S., Karczewski, J. F., Morand, M. (1996) The effects of the atmospheric pressure changes on seismic signals or how to improve the quality of a station. Bull. Seismol. Soc. Am. **86**, 1760–1769.

97) Zürn, W., Widmer, R. (1995) On noise reduction in vertical seismic records below 2 mHz using local barometric pressure. Geophys. Res. Lett. **22**, 3537–3540.

98) Cessaro, R. K., Chan, W. W. (1989) Wide-Angle Triangulation Array Study of Simultaneous Primary Microseism Sources. J. Geophys. Res. **94**, 15555–15563.

99) Haubrich, R. A., McCamy, K. (1969) Microseisms: Coastal and pelagic sources. Rev. Geophys. **7**, 539–571.

100) Juretzek, C., Hadziioannou, C. (2016) Where do ocean microseisms come from? A study of Love-to-Rayleigh wave ratios. J. Geophys. Res. **121**, 6741–6756.

101) Yang, Y., Ritzwoller, M. H. (2008) Characteristics of ambient seismic noise as a source for surface wave tomography. Geochem. Geophys. Geosyst. **9**, Q02008.

102) Tian, Y., Ritzwoller, M. H. (2015) Directionality of ambient noise on the Juan de Fuca plate: Implications for source locations of the primary and secondary microseisms. Geophys. J. Int. **201**, 429–443.

103) Kimman, W. P., Campman, X., Trampert, J. (2012) Characteristics of Seismic Noise: Fundamental and Higher Mode Energy Observed in the Northeast of the Netherlands. Bull. Seismol. Soc. Am. **102**, 1388–1399.

104) Matsuzawa, T., Obara, K., Maeda, T., Asano, Y., Saito, T. (2012) Love- and Rayleigh-Wave Microseisms Excited by Migrating Ocean Swells in the North Atlantic Detected in Japan and Germany. Bull. Seismol. Soc. Am. **102**, 1864–1871.

105) Behr, Y., Townend, J., Bowen, M., Carter, L., Gorman, R., Brooks, L., Bannister, S. (2013) Source directionality of ambient seismic noise inferred from three-component beamforming. J. Geophys. Res. **118**, 240–248.

106) Ruigrok, E., Campman, X., Wapenaar, K. (2011) Extraction of P-wave reflections from microseisms. Comptes Rendus Geoscience **343**, 512–525.

107) Schimmel, M., Stutzmann, E., Gallart, J. (2011) Using instantaneous phase coherence for signal extraction from ambient noise data at a local to a global scale. Geophys. J. Int. **184**, 494–506.

108) Chevrot, S., Sylvander, M., Benahmed, S., Ponsolles, C., Lefèvre, J. M., Paradis, D. (2007) Source locations of secondary microseisms in western Europe: Evidence for both coastal and pelagic sources. J. Geophys. Res. **112**, 1–19.

109) Landès, M., Hubans, F., Shapiro, N. M., Paul, A., Campillo, M. (2010) Origin of deep ocean microseisms by using teleseismic body waves. J. Geophys. Res. **115**, B05302.

110) Gal, M., Reading, A. M., Ellingsen, S. P., Gualtieri, L., Koper, K. D., Burlacu, R., Tkalčić, H., Hemer, M. A. (2015) The frequency dependence and locations of short-period microseisms generated in the Southern Ocean and West Pacific. J. Geophys. Res. **120**, 5764–5781.

111) Stutzmann, E., Ardhuin, F., Schimmel, M., Mangeney, A., Patau, G. (2012) Modelling long-term seismic noise in various environments. Geophys. J. Int. **191**, 707–722.

112) Gualtieri, L., Stutzmann, E., Capdeville, Y., Ardhuin, F., Schimmel, M., Mangeney, A., Morelli, A. (2013) Modelling secondary microseismic noise by normal mode summation. Geophys. J. Int. **193**, 1732–1745.

113) Ardhuin, F., Gualtieri, L., Stutzmann, E. (2015) How ocean waves rock the Earth: Two mechanisms explain microseisms with periods 3 to 300 s. Geophys. Res. Lett. **42**, 765–772.

114) Neale, J., Harmon, N., Srokosz, M. (2017) Monitoring remote ocean waves using P-wave microseisms. J. Geophys. Res. **122**, 470–483.

115) Bromirski, P. D., Duennebier, F. K., Stephen, R. A. (2005) Mid-ocean microseisms. Geochem. Geophys. Geosyst. **6**, Q04009.

116) Reading, A. M., Koper, K. D., Gal, M., Graham, L. S., Tkalčić, H., Hemer, M. A. (2014) Dominant seismic noise sources in the Southern Ocean and West Pacific, 2000-2012, recorded at the Warramunga Seismic Array, Australia. Geophys. Res. Lett. **41**, 3455–3463.

117) Davy, C., Stutzmann, E., Barruol, G., Fontaine, F. R., Schimmel, M. (2015) Sources of secondary microseisms in the Indian Ocean. Geophys. J. Int. **202**, 1180–1189.

118) Gualtieri, L., Stutzmann, E., Farra, V., Capdeville, Y., Schimmel, M., Ardhuin, F., Morelli, A. (2014) Modelling the ocean site effect on seismic noise body waves. Geophys. J. Int. **197**, 1096–1106.

119) Toksöz, M. N., Lacoss, R. T. (1968) Microseisms: Mode Structure and Sources. Science **159**, 872–873.

120) Vinnik, L. (1973) Sources of microseismic P waves. Pure Appl. Geophys. **103**, 282–289.

121) Nishida, K. (2014) Source spectra of seismic hum. Geophys. J. Int. **199**, 416–429.

122) Oliver, J. (1961) On the long period character of shear waves. Bull. Seismol. Soc. Am. **51**, 1–12.

123) Nishida, K. (2013) Global propagation of body waves revealed by cross-correlation analysis of seismic hum. Geophys. Res. Lett. **40**, 1691–1696.

124) Nishida, K., Kobayashi, N., Fukao, Y. (2002) Origin of Earth's ground noise from 2 to 20 mHz. Geophys. Res. Lett. **29**, 52-1-52-4.

125) Nishida, K., Kobayashi, N., Fukao, Y. (2014) Background Lamb waves in the Earth's atmosphere. Geophys. J. Int. **196**, 312–316.

126) Aki, K. (1957) Space and time Spectra of stationary stochastic waves, with special reference to microseisms. Bull. Earthq. Res. Inst. **35**, 415–457.

127) Nishida, K., Kawakatsu, H., Obara, K. (2008) Three-dimensional crustal S wave velocity structure in Japan using microseismic data recorded by Hi-net tiltmeters. J. Geophys. Res. **113**, B10302.

128) Brooks, L. A., Townend, J., Gerstoft, P., Bannister, S., Carter, L. (2009) Fundamental and higher-mode Rayleigh wave characteristics of ambient seismic noise in New Zealand. Geophys. Res. Lett. **36**, 2–6.

129) Poli, P., Pedersen, H. A., Campillo, M. (2012) Emergence of body waves from cross-correlation of short period seismic noise. Geophys. J. Int. **188**, 549–558.

130) Poli, P., Campillo, M., Pedersen, H. (2012) Body-Wave Imaging of Earth's Mantle Discontinuities from Ambient Seismic Noise. Science (80-.). **338**, 1063–1065.

131) Zhan, Z., Ni, S., Helmberger, D. V., Clayton, R. W. (2010) Retrieval of Moho-reflected shear wave arrivals from ambient seismic noise. Geophys. J. Int. **182**, 408–420.

132) Tibuleac, I. M., Seggern, von , D. (2012) Crust-mantle boundary reflectors in Nevada from ambient seismic noise autocorrelations. Geophys. J. Int. **189**, 493–500.

133) Hillers, G., Campillo, M., Ben-Zion, Y., Landès, M. (2013) Interaction of microseisms with crustal heterogeneity: A case study from the San Jacinto fault zone area. Geochem. Geophys. Geosyst. **14**, 2182–2197.

134) Sato, H., Fehler, M. C., Maeda, T. (2012) *Seismic wave propagation and scattering in the heterogeneous earth*, Springer.

135) Scholte, J. G. (1958) Rayleigh waves in isotropic and anisotropic elastic media. Meded. en Verhand. KNMI **72**, 9–43.

136) Harmon, N., Forsyth, D., Webb, S. (2007) Using ambient seismic noise to determine short-period phase velocities and shallow shear velocities in young oceanic lithosphere. Bull. Seismol. Soc. Am. **97**, 2009–2023.

137) Takeo, A., Nishida, K., Isse, T., Kawakatsu, H., Shiobara, H., Sugioka, H., Kanazawa, T. (2013) Radially anisotropic structure beneath the Shikoku Basin from broadband surface wave analysis of ocean bottom seismometer records. J. Geophys. Res. **118**, 2878–2892.

138) Takeo, A., Forsyth, D. W., Weeraratne, D. S., Nishida, K. (2014) Estimation of azimuthal anisotropy in the NW Pacific from seismic ambient noise in seafloor records. Geophys. J. Int. **199**, 11–22.

139) Yao, H., Gouédard, P., Collins, J. A., McGuire, J. J., Hilst, van der , R. D. (2011) Structure of young East Pacific Rise lithosphere from ambient noise correlation analysis of fundamental- and higher-mode Scholte-Rayleigh waves. Comptes Rendus Geoscience **343**, 571–583.

140) Tonegawa, T., Fukao, Y., Takahashi, T., Obana, K., Kodaira, S., Kaneda, Y. (2015) Ambient seafloor noise excited by earthquakes in the Nankai subduction zone. Nature commun. **6**, 6132.

141) Kurrle, D., Widmer-Schnidrig, R. (2008) The horizontal hum of the Earth: A global background of spheroidal and toroidal modes. Geophys. Res. Lett. **35**, 1–5.

142) Ekström, G. (2001) Time domain analysis of Earth's long-period background seismic radiation. J. Geophys. Res. **106**, 26483–26.

143) Saito, T. (2010) Love-wave excitation due to the interaction between a propagating ocean wave and the sea-bottom topography. Geophys. J. Int. **182**, 1515–1523.

144) Tanimoto, T., Lin, C.-j., Hadziioannou, C., Igel, H., Vernon, F. (2016) Estimate of Rayleigh-to-Love wave ratio in the secondary microseism by a small array at Piñon Flat observatory, California. Geophys. Res. Lett. **43**, 173–181.

145) Tanimoto, T., Hadziioannou, C., Igel, H., Wassermann, J., Schreiber, U., Gebauer, A. (2015) Estimate of Rayleigh-to-Love wave ratio in the secondary microseism by colocated ring laser and seismograph. Geophys. Res. Lett. **42**, 2650–2655.

146) Tanimoto, T., Hadziioannou, C., Igel, H., Wassermann, J., Schreiber, U., Gebauer, A., Chow, B. (2016) Seasonal variations in the Rayleigh-to-Love wave ratio in the secondary microseism from colocated ring laser and seismograph. J. Geophys. Res. **121**, 2447–2459.

147) Nakanishi, I. (1992) Rayleigh waves guided by sea-trench topography. Geophys. Res. Lett. **19**, 2385–2388.

148) Yomogida, K. (1992) Fresnel zone inversion for lateral heterogeneities in the earth. Pure Appl. Geophys. **138**, 391–406.

149) Noguchi, S., Maeda, T., Furumura, T. (2013) FDM Simulation of an Anomalous Later Phase from the Japan Trench Subduction Zone Earthquakes. Pure Appl. Geophys. **170**, 95–108.

150) Farra, V., Stutzmann, E., Gualtieri, L., Schimmel, M., Ardhuin, F. (2016) Ray-theoretical modeling of secondary microseism P waves. Geophys. J. Int. **206**, 1730–1739.

151) Tolman, H. L. (2008) A mosaic approach to wind wave modeling. Ocean Modelling **25**, 35–47.

152) Boué, P., Poli, P., Campillo, M., Pedersen, H., Briand, X., Roux, P. (2013) Teleseismic correlations of ambient seismic noise for deep global imaging of the Earth. Geophys. J. Int. **194**, 844–848.

153) Watada, S., Masters, G. (2001) Oceanic excitation of the continuous oscillations of the earth. Eos Trans. AGU **82**, SS2A-0620.

154) Webb, S. C., Zhang, X., Crawford, W. (1991) Infragravity waves in the deep ocean. J. Geophys. Res. **96**, 2723–2736.

155) Uchiyama, Y., McWilliams, J. C. (2008) Infragravity waves in the deep ocean: Generation, propagation, and seismic hum excitation. J. Geophys. Res. **113**, 1–25.

156) Godin, O. A., Zabotin, N. A., Sheehan, A. F., Yang, Z., Collins, J. A. (2013) Power spectra of infragravity waves in a deep ocean. Geophys. Res. Lett. **40**, 2159–2165.

157) Wunk, W. H. (1949) Surf beats. Trans. Am. Geophys. Union **30**, 849–854.

158) Longuet-Higgins M., Stewart, R. (1962) Radiation stress and mass transport in gravity waves with application to surf-beats. J. Fluid Mech. **13**, 481–504.

159) Herbers, T. H. C., Elgar, S., Guza, R. T. (1995) Generation and propagation of infragravity waves. J. Geophys. Res. **100**, 24863–24782.

160) Bowen, A. J., Guza, R. T. (1978) Edge waves and surf beat. J. Geophys. Res. **83**, 1913–1920.

161) Harmon, N., Henstock, T., Srokosz, M., Tilmann, F., Rietbrock, A., Barton, P. (2012) Infragravity wave source regions determined from ambient noise correlation. Geophys. Res. Lett. **39**, 1–5.

162) Tono, Y., Nishida, K., Fukao, Y., To, A., Takahashi, N. (2014) Source characteristics of ocean infragravity waves in the Philippine Sea: analysis of 3-year continuous network records of seafloor motion and pressure. Earth Planets Space **66**, 99.

163) Rawat, A., Ardhuin, F., Ballu, V., Crawford, W., Corela, C., Aucan, J. (2014) Infragravity waves across the oceans. Geophys. Res. Lett. **41**, 7957–7963.

164) Aucan, J., Ardhuin, F. (2013) Infragravity waves in the deep ocean: An upward revision. Geophys. Res. Lett. **40**, 3435–3439.

165) Ardhuin, F., Rawat, A., Aucan, J. (2014) A numerical model for free infragravity waves: Definition and validation at regional and global scales. Ocean Modelling **77**, 20–32.

166) (2014) A unified theory of microseisms and hum. J. Geophys. Res. **119**, 3317–3339.

167) Webb, S. C. (2008) The earth's hum: The excitation of earth normal modes by ocean waves. Geophys. J. Int. **174**, 542–566.

168) Kobayashi, N., Kusumi, T., Suda, N. (2008) Infrasounds and background free osicllations. *Proc. 8th Int. Conf. Theor. Comput. Acoust*, Taroudakis, M., Papadakis, P., eds., Univ. Crete, Heraklion, Crete, Greece, pp. 105–114.

169) Gossard, E. E., Hooke, W. H. (1975) *Waves in The Atmosphere*, Elsevier Amsterdam.

170) Shimazaki, K., Nakajima, K. (2009) Oscillations of Atmosphere-Solid Earth Coupled System Excited by the Global Activity of Cumulus Clouds. Eos Trans. AGU **90**, SS3A-1734.

171) Darbyshire, J., Okeke, E. O. (1969) A Study of Primary and Secondary Microseisms recorded in Anglesey. Geophys. J. Int. **17**, 63–92.

172) Okeke, E. O., Asor, V. E. (2000) On the microseisms associated with coastal sea waves. Geophys. J. Int. **141**, 672–678.

173) Haubrich, R. A., Munk, W. H., Snodgrass, F. E. (1963) Comparative spectra of microseisms and swell. Bull. Seismol. Soc. Am. **53**, 27–37.

174) Ostrovsky, A., Korhonen, H. (1990) On correlation of the energies of primary and secondary storm microseisms. Phys. Earth Planet. Inter. **63**, 196–200.

175) Friederich, W. (1999) Propagation of seismic shear and surface waves in a laterally heterogeneous mantle by multiple forward scattering. Geophys. J. Int. **136**, 180–204.

176) Beucler, E., Mocquet, A., Schimmel, M., Chevrot, S., Quillard, O., Vergne, J., Erome, Sylvander, M. (2015) Observation of deep water microseisms in the North Atlantic Ocean using tide modulations. Geophys. Res. Lett. **42**, 316–322.

177) Dolenc, D., Romanowicz, B., McGill, P., Wilcock, W. (2008) Observations of infragravity waves at the ocean-bottom broadband seismic stations Endeavour (KEBB) and Explorer (KXBB). Geochem. Geophys. Geosyst. **9**, Q05007.

178) Young, A. P., Guza, R. T., Dickson, M. E., O'Reilly, W. C., Flick, R. E. (2013) Ground motions on rocky, cliffed, and sandy shorelines generated by ocean waves. J. Geophys. Res. **118**, 6590–6602.

179) Sugioka, H., Fukao, Y., Kanazawa, T. (2010) Evidence for infragravity wave-tide resonance in deep oceans. Nature commun. **1**, 84.

180) Bromirski, P. D. (2002) The near-coastal microseism spectrum: Spatial and temporal wave climate relationships. J. Geophys. Res. **107**, 2166.

181) Longuet-Higgins, M. S. (1953) Can Sea Waves Cause Microseisms? Proc. Symposium on Microseisms, Harriman 1952 **306**, 74–93.

182) Wilson, D. K., Frisk, G. V., Lindstrom, T. E., Sellers, C. J. (2003) Measurement and prediction of ultralow frequency ocean ambient noise off the eastern U.S. coast. J. Acoust. Soc. Am. **113**, 3117–3133.

183) Ardhuin, F., Herbers, T. H. C. (2013) Noise generation in the solid Earth, oceans and atmosphere, from nonlinear interacting surface gravity waves in finite depth. J. Fluid Mech. **716**, 316–348.